Nonequilibrium molecular dynamics method based on coarse-graining formalism: Application to a nonuniform temperature field system

Masayuki Uranagase[*] and Shuji Ogata

Department of Physical Science and Engineering, Nagoya Institute of Technology, Nagoya, Aichi 466-8555, Japan

A nonequilibrium molecular dynamics method is proposed to produce nonequilibrium states flexibly. In this method, virtual points are set in a simulation box, and coarse-grained physical quantities at these points are constrained using Gauss's principle of least constraint. The coarse-grained physical quantities are evaluated by averaging microscopic quantities with an appropriate weight. To obtain the weight to evaluate the coarse-grained physical quantities, a shape function matrix is initially constructed from the particle configuration. This matrix expresses an interpolation of the physical quantities at particle positions from the coarse-grained quantities at the virtual points. Then, a matrix form of the weight is calculated as the Moore-Penrose pseudoinverse matrix for the shape function matrix. This method is applied to constrain the coarse-grained kinetic energy and produce a nonuniform temperature field in the system. The temperature profile at a nonequilibrium steady state depends on the method for constructing the shape function matrix. In particular, a local temperature coincides with the coarse-grained temperature when the shape function matrix is constructed based on a higher-order interpolation.

I. INTRODUCTION

Atomistic-scale simulations such as molecular dynamics (MD) [1,2] and Monte Carlo simulations [1,3] are effective tools for understanding physical, chemical, and biological phenomena at the microscopic level. In the MD simulation, dynamical properties can be analyzed by numerically integrating equations of motion of particles in a system. If there is no external field, then a simple application of this method conserves the system's total energy, i.e., physical quantities are obtained as statistical averages under a microcanonical ensemble. In general, a large system is required to identify the microcanonical ensemble with other realistic situations such as constant temperature and/or constant pressure. Extensive methods, such as thermostats [4–6] and barostats [7–9], are developed to perform MD simulations in realistic situations with limited computational resources.

Investing in the development of MD methods is not limited to the equilibrium case. MD simulations have a wide range of applications in nonequilibrium situations [10,11]. Equilibrium MD simulations can be applied to evaluate linear transport coefficients using the Green-Kubo relation [12,13]. In addition, various methods to directly treat nonequilibrium states in the simulation are also developed to study properties far from equilibrium. In fluid flow analyses, homogeneous shear flow can be produced by applying boundary-driven methods, e.g., an external force is exerted on particles in fluid like wall regions [14]. For a system with a periodic boundary condition, the Lees-Edwards method is applicable [15]. Sophisticated methods such as the DOLLS tensor [16] and the SLLOD algorithm [17] are formulated to combine the re-

sponse theory, which is not established in the boundary-driven methods. Moreover, methods for producing inhomogeneous flow are also developed. For example, the shear viscosity is evaluated by applying sinusoidal shear flow to the system [18].

Another important application of nonequilibrium MD simulations is the analysis of properties related to thermal transport [19]. A simple method to produce a temperature gradient is by inserting the system between two thermostats with different temperatures [20]. This method can easily be applied to inhomogeneous systems, e.g., grain boundaries [21,22] and interfaces between different materials [23]. In addition, a method for producing the temperature gradient of systems with periodic boundary conditions is also developed [24]. Another strategy to study thermal transport is to add a fictitious field to the system to produce heat flux without the temperature gradient [25,26]. This method enables efficient calculation of thermal conductivity based on the linear response theory [13] and is applicable to systems with periodic boundary conditions since this method produces a homogeneous state.

Nonequilibrium MD simulations are often combined with constraint methods. Gauss's principle of least constraint [27] provides the steps for calculating constraint forces in simulations with constraints. Evans *et al.* [28] developed a method to realize a thermostat in MD simulations based on this principle where the heat generated under a nonequilibrium state can be removed using this thermostat. The constraint method utilizing Gauss's principle of least constraint possesses the advantage that different physical quantities can be treated similarly. Isokinetic nonequilibrium methods with additional constraints, e.g., pressure [29], stress [30], and particle current [28], are also formulated using Gauss's principle of least constraint.

_____

[*]uranagase.masayuki@nitech.ac.jp

The existing methods for the nonequilibrium MD simulations mentioned above contribute to a thorough understanding of nonequilibrium phenomena. For instance, these methods lead to the discovery of nontrivial relations satisfied in nonequilibrium states [31,32]. However, in a realistic situation, various nonequilibrium states can be generated. More effort should be devoted to developing a method that enables the flexible production of nonequilibrium states in the MD simulations to mimic realistic nonequilibrium situations.

One of the strategies for flexibly producing nonequilibrium states is to control local physical quantities in the simulation by adopting the constraint method. Galea *et al.* [33] derived non-Hamiltonian equations of motion for general constraints based on the geometric principle of least constraint, which includes Gauss's principle of least constraint in a certain limit. In their work, isokinetic shear flow is generated by applying it to the total momenta constraints in two regions. In addition, Smith *et al.* [34] recently proposed a method for controlling a fluid's local momentum based on the control volume formulation [35]. In the existing methods for constraining local physical quantities, physical quantities averaged over a local region are usually adopted as the local values of them. Since the physical quantity varies in the local region, there is ambiguity in the sense that the place where the local physical quantity coincides with the designated value cannot be determined in advance. This ambiguity may cause production of an undesirable nonequilibrium state, e.g., a range of variation in the physical quantity in the system differs from what is expected. This feature, which is pronounced for cases with few constraints, is inconvenient for controlling nonequilibrium states. To avoid this inconvenience, it is preferable to develop the method for designating the local physical quantities at points in the system.

In this paper, we propose a method for controlling the local physical quantities at points in the system to produce nonequilibrium states flexibly. This method involves the placement of virtual points in the system, and coarse-grained physical quantities at each virtual point are calculated as the average of microscopic physical quantities, which are defined for each particle in the system, with an appropriate weight. Then, the coarse-grained physical quantities at the virtual points are constrained by applying constraint forces derived from Gauss's principle of least constraint. In theory, it is desirable to incorporate physical quantity fluctuations, which are neglected in the constraint method. However, it is not easy to determine appropriate fluctuations of the coarse-grained physical quantities under the nonequilibrium states. On the other hand, the formulation based on the constraint method can systematically be conducted because Gauss's principle of least constraint enables the treatment of various quantities in the same manner as stated above. Therefore, we adopt the constraint method with Gauss's principle of least constraint as a first step for constructing the method. The present method is applied to a two-dimensional system that interacts via the Weeks-Chandler-Andersen (WCA) potential [36] in a nonuniform temperature field.

This paper is organized as follows. Section II describes the details of our method. First, we discuss the weight construction for averaging the microscopic physical quantity. Next, the constraint force calculation and its application to the kinetic energy constraint are explained. We also discuss the computational implementation of the present method. Section III describes the results obtained by applying the present method to a two-dimensional system that interacts via the WCA potential. Then, we show that if the weight is appropriately constructed, local temperatures at the virtual points are approximately equal to the corresponding coarse-grained temperatures in the case of one-dimensional and two-dimensional temperature nonuniformity. Finally, our conclusions are given in Sec. IV.

II. METHOD

A. Weight function for coarse-graining a physical quantity

We consider a region Ω in D-dimensional space and assume that the physical quantity A, such as momentum and temperature, is well defined in Ω. These values are given at N_{VP} virtual points within Ω: A_I represents the value of A at the Ith virtual point. Then, a simple estimate of A at any point $\omega \in \Omega$ is provided by a linear combination of the physical quantity at the virtual points:

$$A(\omega) = \sum_{I=1}^{N_{\mathrm{VP}}} s_I(\omega) A_I, \quad \sum_{I=1}^{N_{\mathrm{VP}}} s_I(\omega) = 1, \tag{1}$$

where $s_I(\omega)$, regarded as the weight for the Ith virtual point, is not limited to positive values. For example, using Delaunay triangulation [37], Ω is divided into simplices whose vertices correspond to the virtual points. A point's coordinate inside the simplex is given by a linear combination of the simplex vertices, where the sum of the coefficients equals 1. When the same coefficient is applied to the physical quantity A, $A(\omega)$ for any point $\omega \in \Omega$ can be expressed in the form of Eq. (1).

Here, we consider the case where particles obeying Newtonian mechanics are contained in Ω where the number N of particles is sufficiently greater than the number N_{VP} of virtual points. The ith particle's position, velocity, and acceleration are denoted by $\mathbf{r}_i$, $\dot{\mathbf{r}}_i$, and $\ddot{\mathbf{r}}_i$, respectively. We assume that a microscopic physical quantity associated with A can be defined for all particles and that the value of the ith particle's microscopic physical quantity is given by a_i. When the physical quantity in Ω is expressed as Eq. (1), the microscopic physical quantity is written as

$$\mathbf{a} = \mathcal{S}\mathbf{A}, \tag{2}$$

where $\mathbf{a} = (a_1, \cdots, a_N)^T$ and $\mathbf{A} = (A_1, \cdots, A_{N_{\mathrm{VP}}})^T$, in which superscript T signifies the matrix transpose, and $\mathcal{S}$ is an $N \times N_{\mathrm{VP}}$ matrix. Hereafter, we refer to $\mathcal{S}$ and its entry as a shape function matrix and a shape function, respectively, as used in the finite element method [38]. Since Eq. (2) is derived from Eq. (1), $\mathcal{S}$ satisfies the relation $\sum_{J=1}^{N_{\mathrm{VP}}} \mathcal{S}_{iJ} = 1$ for all i, where $\mathcal{S}_{iJ}$ is the (i, J) entry of $\mathcal{S}$.

Then, our goal is to evaluate the coarse-grained physical quantity values at N_{VP} virtual points when the microscopic physical quantities for N particles are given. We assume that $\mathbf{A}$ is written as a linear function of $\mathbf{a}$:

$$\mathbf{A} = \mathcal{W}\mathbf{a}, \tag{3}$$

where $\mathcal{W}$, which is an $N_{\mathrm{VP}} \times N$ matrix, and its entry are called a weight function matrix and a weight function, respectively.

By substituting Eq. (2) into Eq. (3), we obtain

$$\boldsymbol{A} = \mathcal{W}\mathcal{S}\boldsymbol{A}. \tag{4}$$

This relation holds irrespective of $\boldsymbol{A}$ when $\mathcal{W}\mathcal{S}$ equals the $N_{VP} \times N_{VP}$ unit matrix. If $\mathcal{W}\mathcal{S}$ is the unit matrix, then $\sum_{k=1}^{N} \mathcal{W}_{Ik}\mathcal{S}_{kJ} = \delta_{IJ}$, where δ_{IJ} represents the Kronecker's δ, i.e., δ_{IJ} equals 1 if $I = J$, and 0 otherwise. Since $\sum_{J=1}^{N_{VP}} \mathcal{S}_{kJ} = 1$, $\sum_{J=1}^{N_{VP}} \sum_{k=1}^{N} \mathcal{W}_{Ik}\mathcal{S}_{kJ} = \sum_{k=1}^{N} \mathcal{W}_{Ik}(\sum_{J=1}^{N_{VP}} \mathcal{S}_{kJ}) = \sum_{k=1}^{N} \mathcal{W}_{Ik}$. Moreover, $\sum_{J=1}^{N_{VP}} \delta_{IJ} = 1$. From these relations, we obtain

$$\sum_{k=1}^{N} \mathcal{W}_{Ik} = 1. \tag{5}$$

A natural choice of $\mathcal{W}$ to satisfy Eq. (4) is as follows:

$$\mathcal{W} = (\mathcal{S}^T \mathcal{S})^{-1} \mathcal{S}^T. \tag{6}$$

This matrix, also known as the Moore-Penrose pseudoinverse matrix [39], plays an essential role in coarse-grained particle MD simulations [40,41]. A different approach to derivation of Eq. (6) is to obtain $\mathcal{W}$ which minimizes $(\mathcal{S}\mathcal{W}\boldsymbol{a} - \boldsymbol{a})^T (\mathcal{S}\mathcal{W}\boldsymbol{a} - \boldsymbol{a})$ [40]. Appendix A contains details of the derivation via this minimization. It should be noted that $\mathcal{S}\mathcal{W}$ is generally not a unit matrix. We also notice that $\mathcal{W}$ depends on the particle's configuration, meaning that, even if a particle is fixed, the weight associated with it varies as other particles move. To evaluate the coarse-grained physical quantities at the virtual points in Ω, we use $\mathcal{W}$ defined by Eq. (6).

B. Gauss's principle of least constraint

We consider a system containing N particles with N_c constraints. The Ith constraint condition is assumed to be $B_I(\{\boldsymbol{r}\}, \{\dot{\boldsymbol{r}}\}, t) = 0$, where $\{\boldsymbol{r}\}$ and $\{\dot{\boldsymbol{r}}\}$ signify a set of particle positions and velocities, respectively. If only one coarse-grained physical quantity A is constrained at N_{VP} virtual points, then $N_c = N_{VP}$ and $B_I(\{\boldsymbol{r}\}, \{\dot{\boldsymbol{r}}\}, t)$ is written from the result in Sec. II A as

$$B_I(\{\boldsymbol{r}\}, \{\dot{\boldsymbol{r}}\}, t) \equiv \sum_{j=1}^{N} \mathcal{W}_{Ij}(\{\boldsymbol{r}\}) a_j(\{\boldsymbol{r}\}, \{\dot{\boldsymbol{r}}\}) - A_I(t) = 0, \tag{7}$$

where $A_I(t)$ is the value of A at the Ith virtual point at time t and we explicitly state the $\{\boldsymbol{r}\}$ and $\{\dot{\boldsymbol{r}}\}$ dependence of $\mathcal{W}$ and $\boldsymbol{a}$.

The constraint is nonholonomic when B_I depends on the particle velocities. In this case, by taking the first derivative of B_I with respect to time, the equation that the particle acceleration $\{\ddot{\boldsymbol{r}}\}$ should satisfy is obtained as

$$\sum_{i=1}^{N} \ddot{\boldsymbol{r}}_i \cdot \boldsymbol{b}_{I,i}(\{\boldsymbol{r}\}, \{\dot{\boldsymbol{r}}\}, t) + c_I(\{\boldsymbol{r}\}, \{\dot{\boldsymbol{r}}\}, t) = 0, \tag{8}$$

where $\boldsymbol{b}_{I,i}(\{\boldsymbol{r}\}, \{\dot{\boldsymbol{r}}\}, t) = \partial B_I / \partial \dot{\boldsymbol{r}}_i$ and $c_I(\{\boldsymbol{r}\}, \{\dot{\boldsymbol{r}}\}, t) = \sum_{i=1}^{N} \dot{\boldsymbol{r}}_i \cdot \partial B_I / \partial \boldsymbol{r}_i + \partial B_I / \partial t$. The constraint becomes holonomic when B_I is independent of the velocities. For the holonomic constraint, an equation that has the same form as Eq. (8) can be obtained by taking the second derivative of B_I with respect to time, although, the expressions of $\boldsymbol{b}_{I,i}(\{\boldsymbol{r}\}, \{\dot{\boldsymbol{r}}\}, t)$ and $c_I(\{\boldsymbol{r}\}, \{\dot{\boldsymbol{r}}\}, t)$ differ from the case of the nonholonomic constraint.

The equation of motion for the ith particle is given by

$$\ddot{\boldsymbol{r}}_i = \frac{\boldsymbol{F}_i + \boldsymbol{G}_i}{m_i}, \tag{9}$$

where $\boldsymbol{F}_i$ denotes force acting on the ith particle when no constraint exists, $\boldsymbol{G}_i$ is constraint force for the ith particle, i.e., the additional force required to meet the constraint conditions, and m_i is the mass of the ith particle. The equation to calculate $\boldsymbol{G}_i$ is obtained by substituting Eq. (9) into Eq. (8), which is given as

$$\sum_{i=1}^{N} \left(\frac{\boldsymbol{F}_i + \boldsymbol{G}_i}{m_i} \right) \cdot \boldsymbol{b}_{I,i}(\{\boldsymbol{r}\}, \{\dot{\boldsymbol{r}}\}, t) + c_I(\{\boldsymbol{r}\}, \{\dot{\boldsymbol{r}}\}, t) = 0, \tag{10}$$

However, another condition must be met to determine the unique $\boldsymbol{G}_i$. Gauss's principle of least constraint [27] is a well-known requirement for determining the unique $\boldsymbol{G}_i$. Under the constraints, this principle requires the minimization of $\sum_{i=1}^{N} \boldsymbol{G}_i \cdot \boldsymbol{G}_i / 2m_i$. Taking the constraints into account, an objective function that should be minimized is written by

$$\sum_{i=1}^{N} \frac{\boldsymbol{G}_i \cdot \boldsymbol{G}_i}{2m_i} + \sum_{I=1}^{N_c} \zeta_I \left\{ \sum_{i=1}^{N} \boldsymbol{b}_{I,i}(\{\boldsymbol{r}\}, \{\dot{\boldsymbol{r}}\}, t) \right. $$
$$\left. \cdot \left(\frac{\boldsymbol{F}_i + \boldsymbol{G}_i}{m_i} \right) + c_I(\{\boldsymbol{r}\}, \{\dot{\boldsymbol{r}}\}, t) \right\}, \tag{11}$$

where ζ_I denotes a Lagrange multiplier associated with the Ith constraint condition. When Eq. (11) is minimized, its derivative with respect to $\boldsymbol{G}_i$ becomes 0. Hence, $\boldsymbol{G}_i$ is computed as

$$\boldsymbol{G}_i = -\sum_{I=1}^{N_c} \zeta_I \boldsymbol{b}_{I,i}(\{\boldsymbol{r}\}, \{\dot{\boldsymbol{r}}\}, t). \tag{12}$$

By substituting Eq. (12) into Eq. (10), the equation for ζ_I can be written as

$$\mathcal{B}\boldsymbol{\zeta} = \boldsymbol{w}, \tag{13}$$

where $\boldsymbol{\zeta} = (\zeta_1, \cdots, \zeta_{N_c})^T$, $\mathcal{B}$ is the $N_c \times N_c$ matrix whose (α, β) entry is given by

$$\mathcal{B}_{\alpha\beta} = \sum_{i=1}^{N} \frac{\boldsymbol{b}_{\alpha,i}(\{\boldsymbol{r}\}, \{\dot{\boldsymbol{r}}\}, t) \cdot \boldsymbol{b}_{\beta,i}(\{\boldsymbol{r}\}, \{\dot{\boldsymbol{r}}\}, t)}{m_i}, \tag{14}$$

and $\boldsymbol{w}$ is the N_c-dimensional vector whose αth component w_α is given by

$$w_\alpha = c_\alpha(\{\boldsymbol{r}\}, \{\dot{\boldsymbol{r}}\}, t) + \sum_{i=1}^{N} \frac{\boldsymbol{F}_i \cdot \boldsymbol{b}_{\alpha,i}(\{\boldsymbol{r}\}, \{\dot{\boldsymbol{r}}\}, t)}{m_i}. \tag{15}$$

The constraint force can be calculated by solving Eq. (13) to obtain the Lagrange multipliers and substituting them into Eq. (12). Notably, this formulation is easily extended to cases where multiple physical quantities are constrained and/or additional constraints are applied.

C. Application to the constraint of kinetic temperature at virtual points

In this study, the kinetic energy is adopted as the physical quantity controlled in simulations to produce a nonuniform

temperature field. The kinetic energy constraint condition at the Ith virtual point is written as

$$B_I(\{\mathbf{r}\}, \{\dot{\mathbf{r}}\}, t) = \sum_{j=1}^{N} \mathcal{W}_{Ij}(\{\mathbf{r}\}) m_j \dot{\mathbf{r}}_j \cdot \dot{\mathbf{r}}_j - D k_B T_I(t) = 0, \quad (16)$$

where k_B is Boltzmann's constant and T_I signifies the coarse-grained kinetic temperature at the Ith virtual point. In this work, instantaneous velocity values are used to evaluate the coarse-grained kinetic energy. This is plausible when only the coarse-graining in space is considered. If the coarse-graining in time is also adopted, then the analysis using MD simulations and the lattice Boltzmann method indicates that the average velocity may be appropriate for obtaining coarse-grained physical quantities [42]. We refer to the kinetic temperature as the temperature hereafter, though there are multiple expressions for temperature [43], which often provide different values at a nonequilibrium state [44,45]. For the constraint written by Eq. (16), $\mathbf{b}_{I,i}(\{\mathbf{r}\}, \{\dot{\mathbf{r}}\})$ is calculated as

$$\mathbf{b}_{I,i}(\{\mathbf{r}\}, \{\dot{\mathbf{r}}\}) = 2\mathcal{W}_{Ii}(\{\mathbf{r}\}) m_i \dot{\mathbf{r}}_i. \quad (17)$$

That is, $\mathbf{b}_{I,i}$ is proportional to the ith particle velocity.

Consider the simplest case, in which the temperature is given at only one virtual point in the system. $\mathcal{S}_{i1} = 1$ for all i in this case. According to Eq. (6), the weight functions for all the particles are the same, i.e., $\mathcal{W}_{1i} = 1/N$ for all i. When $\mathcal{W}$ is substituted into Eq. (16), the constraint condition is $\sum_{j=1}^{N} m_j \dot{\mathbf{r}}_j \cdot \dot{\mathbf{r}}_j - N D k_B T_1(t) = 0$. This equation is the condition used in the Gaussian thermostat [28]. Therefore, the Gaussian thermostat is the simplest case in our method.

When the kinetic energy is controlled at the multiple virtual points in the system, $\mathcal{W}$ depends on the particle configuration. For this case, $c_I(\{\mathbf{r}\}, \{\dot{\mathbf{r}}\}, t)$ in Eq. (11) is given by

$$c_I(\{\mathbf{r}\}, \{\dot{\mathbf{r}}\}, t) = \sum_{i=1}^{N} \left(\sum_{j=1}^{N} \frac{\partial \mathcal{W}_{Ij}(\{\mathbf{r}\})}{\partial \mathbf{r}_i} m_j \dot{\mathbf{r}}_j \cdot \dot{\mathbf{r}}_j \right) \cdot \dot{\mathbf{r}}_i$$
$$- D k_B \frac{\partial T_I(t)}{\partial t}. \quad (18)$$

Since Eq. (6) gives $\mathcal{W}$, the differentiation of $\mathcal{W}_{Ij}$ is written as

$$\frac{\partial \mathcal{W}_{Ij}}{\partial r_{i,\alpha}} = \sum_{K=1}^{N_{\mathrm{VP}}} \frac{\partial [(\mathcal{S}^T \mathcal{S})^{-1}]_{IK}}{\partial r_{i,\alpha}} (\mathcal{S}^T)_{Kj}$$
$$+ \sum_{K=1}^{N_{\mathrm{VP}}} [(\mathcal{S}^T \mathcal{S})^{-1}]_{IK} \frac{\partial (\mathcal{S}^T)_{Kj}}{\partial r_{i,\alpha}}, \quad (19)$$

where $r_{i,\alpha}$ represents the αth component of $\mathbf{r}_i$. In Eq. (19), the first term on the right-hand side is calculated using the relation $\partial \mathcal{M}^{-1}/\partial x = -\mathcal{M}^{-1}(\partial \mathcal{M}/\partial x)\mathcal{M}^{-1}$ for a regular matrix $\mathcal{M}$ which is a function of x. After some algebra, we obtain

$$\frac{\partial \mathcal{W}_{Ij}}{\partial r_{i,\alpha}} = \sum_{K=1}^{N_{\mathrm{VP}}} [(\mathcal{S}^T \mathcal{S})^{-1}]_{IK}$$
$$\times \left\{ \frac{\partial \mathcal{S}_{jK}}{\partial r_{i,\alpha}} - \sum_{P=1}^{N_{\mathrm{VP}}} \sum_{q=1}^{N} \left(\frac{\partial \mathcal{S}_{qK}}{\partial r_{i,\alpha}} \mathcal{S}_{qP} + \mathcal{S}_{qK} \frac{\partial \mathcal{S}_{qP}}{\partial r_{i,\alpha}} \right) \mathcal{W}_{Pj} \right\}. \quad (20)$$
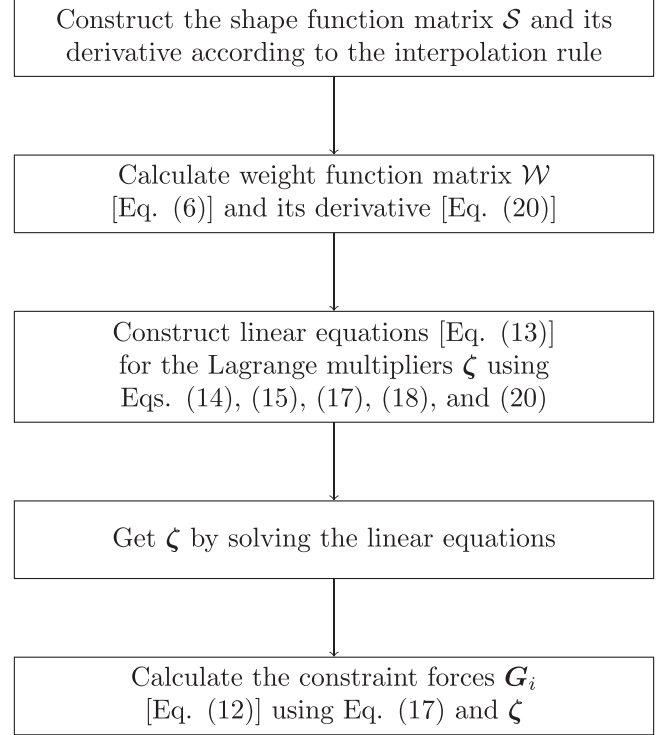
FIG. 1. The flowchart of constraint force calculation.

$c_I(\{\mathbf{r}\}, \{\dot{\mathbf{r}}\}, t)$ is obtained by substituting Eq. (20) into Eq. (18). The constraint force can be evaluated using Eqs. (13)–(15) with $\mathbf{b}_{I,i}(\{\mathbf{r}\}, \{\dot{\mathbf{r}}\})$ and $c_I(\{\mathbf{r}\}, \{\dot{\mathbf{r}}\}, t)$ obtained here.

D. Computational details

This subsection explains a tangible way to apply the present method in an MD simulation code. Before starting the simulation, we define the positions of the virtual points, where the coarse-grained physical quantities are constrained. Then, we must define a rule for interpolating the physical quantities at any point in a simulation box from those at the virtual points, i.e., the calculation method for the weight in Eq. (1). The rule choice affects the nonequilibrium state that is produced, as shown in Sec. III. The calculation of the constraint force is conducted according to the flowchart in Fig. 1. First, we construct the shape function matrix from the particle configuration according to the interpolation rule defined in advance. Then, the weight function matrix can be calculated from the shape function matrix by Eq. (6) and $\mathbf{b}_{I,i}(\{\mathbf{r}\}, \{\dot{\mathbf{r}}\})$ is obtained by substituting the weight function into Eq. (17). Moreover, the shape and the weight function matrices and their derivatives are used to construct the linear equations for the Lagrange multipliers given in Eq. (13). The Lagrange multipliers obtained by solving the linear equations are substituted into Eq. (12) to obtain the constraint force acting on the particles.

In the MD simulations, the equations of motion are numerically integrated to allow the system to evolve. The velocity Verlet method [46] is frequently used for the numerical integration of the equations of motion. If the present method is

applied with the velocity Verlet method, then the position and the velocity of the ith particle are updated as

$$\boldsymbol{r}_i(t + \delta t) = \boldsymbol{r}_i(t) + \delta t \dot{\boldsymbol{r}}_i(t) + \frac{(\delta t)^2}{2m_i}[\boldsymbol{F}_i(t) + \boldsymbol{G}_i(t)], \quad (21)$$

$$\dot{\boldsymbol{r}}_i(t + \delta t) = \dot{\boldsymbol{r}}_i(t) + \frac{\delta t}{2m_i}[\boldsymbol{F}_i(t) + \boldsymbol{G}_i(t)$$
$$+ \boldsymbol{F}_i(t + \delta t) + \boldsymbol{G}_i(t + \delta t)], \quad (22)$$

where δt is the time step used for integrating the equations of motion. Since $\boldsymbol{G}_i(t + \delta t)$ depends on the particle velocities at $t + \delta t$ as mentioned above, Eq. (22) possesses a self-consistent form. Then, an iteration method must be applied to solve the self-consistent equation for the velocities. However, it is not necessary to apply the iteration method to update the positions, indicating that the shape and weight function matrices, as well as the interaction force, should be calculated only once every MD step.

In nonequilibrium MD simulations, higher-order integration schemes without symplecticity are often adopted instead of the velocity Verlet method. This is because the importance of the symplecticity decreases for nonequilibrium situations, and it is necessary to evaluate the positions and the velocities with high accuracy. One of these schemes is the fourth-order Runge-Kutta method. If the differential equation is given by $dz(t)/dt = f(z, t)$, then $z(t)$ is updated in the fourth-order Runge-Kutta method as

$$z(t + \delta t) = z(t) + \delta t \sum_{\alpha=1}^{4} \xi_\alpha f_\alpha$$

$$f_\alpha = f\left(z(t) + \delta t \sum_{\beta=1}^{4} \gamma_{\alpha\beta} f_\beta, t + \chi_\alpha \delta t\right), \quad (23)$$

where ξ_α, χ_α, and $\gamma_{\alpha\beta}$ are coefficients determined to attain fourth-order accuracy. Note that these coefficients are not uniquely determined because the conditions to attain fourth-order accuracy are less than the number of the coefficients. The most famous set of coefficients is given by

$$(\xi_1, \xi_2, \xi_3, \xi_4) = \left(\tfrac{1}{6}, \tfrac{1}{3}, \tfrac{1}{3}, \tfrac{1}{6}\right)$$
$$(\chi_1, \chi_2, \chi_3, \chi_4) = (0, 0.5, 0.5, 1)$$
$$\begin{pmatrix} \gamma_{11} & \gamma_{12} & \gamma_{13} & \gamma_{14} \\ \gamma_{21} & \gamma_{22} & \gamma_{23} & \gamma_{24} \\ \gamma_{31} & \gamma_{32} & \gamma_{33} & \gamma_{34} \\ \gamma_{41} & \gamma_{42} & \gamma_{43} & \gamma_{44} \end{pmatrix} = \begin{pmatrix} 0 & 0 & 0 & 0 \\ 0.5 & 0 & 0 & 0 \\ 0 & 0.5 & 0 & 0 \\ 0 & 0 & 1 & 0 \end{pmatrix}. \quad (24)$$

The following is the example of other sets of coefficients:

$$(\xi_1, \xi_2, \xi_3, \xi_4) = \left(\tfrac{1}{8}, \tfrac{3}{8}, \tfrac{3}{8}, \tfrac{1}{8}\right),$$
$$(\chi_1, \chi_2, \chi_3, \chi_4) = \left(0, \tfrac{1}{3}, \tfrac{2}{3}, 1\right),$$
$$\begin{pmatrix} \gamma_{11} & \gamma_{12} & \gamma_{13} & \gamma_{14} \\ \gamma_{21} & \gamma_{22} & \gamma_{23} & \gamma_{24} \\ \gamma_{31} & \gamma_{32} & \gamma_{33} & \gamma_{34} \\ \gamma_{41} & \gamma_{42} & \gamma_{43} & \gamma_{44} \end{pmatrix} = \begin{pmatrix} 0 & 0 & 0 & 0 \\ \tfrac{1}{3} & 0 & 0 & 0 \\ -\tfrac{1}{3} & 1 & 0 & 0 \\ 1 & -1 & 1 & 0 \end{pmatrix}. \quad (25)$$

This set is often called the 3/8-rule. Since the fourth-order Runge-Kutta method with the coefficients given in Eq. (24) or Eq. (25) is an explicit scheme, any iteration scheme for updating the particle positions and velocities is not required.

Instead, both the interatomic and constraint forces must be calculated four times every MD step.

The difficulty in using Gauss's principle of least constraint is that a systematic drift of the constrained value is often induced. In this principle, the constraint is executed using the condition that only the time derivative of the constraint condition equals 0. In MD simulations, its value usually deviates from 0 because the time step for integration is not infinitesimal. If the deviation is completely random, then the constraint value may fluctuate around the designated value. However, the deviation often possesses a certain tendency. Then, the drift of the constraint value occurs as a result of the accumulation of this deviation. The drifts of the constraint values are common in numerical simulations, and various methods have been developed to eliminate them [47–49]. In this work, to satisfy the constraint conditions of Eq. (16), $\partial T_I(t)/\partial t$ in Eq. (18) is adaptively determined by

$$\frac{\partial T_I(t)}{\partial t} = \frac{1}{\delta t}\left[T_I(t + \delta t) \right.$$
$$\left. - \frac{1}{Dk_B} \sum_{i=1}^{N} \mathcal{W}_{Ii}(\{\boldsymbol{r}(t)\}) m_i \dot{\boldsymbol{r}}_i(t) \cdot \dot{\boldsymbol{r}}_i(t) \right], \quad (26)$$

where the first and the second terms in the square bracket signify the target value of the temperature at $t + \delta t$ and the calculated coarse-grained temperature at t, respectively.

Deviations of the constraint values due to drift strongly depend on the method of numerical integration of the equations of motion, as shown in Appendix B. The results in Appendix B demonstrate that the fourth-order Runge-Kutta method with the coefficients given by Eq. (25) is suitable when the time step is sufficiently small. Therefore, we adopt this scheme for numerical integration of the equations of motion performed in Sec. III. Although we apply the adaptive corrections of the constraint values given by Eq. (26), the results in Appendix B imply that the influence of this correction may be negligible for the small time step.

III. RESULTS

In this section, we test the present method for the two-dimensional system. Particles are contained in a two-dimensional box whose dimensions are L_x and L_y in the x and the y directions, respectively. The periodic boundary condition is applied in both directions. The number N of particles is chosen so that an average number density is 0.75. Moreover, the mass m of all the particles is the same. The particles interact via the WCA potential V_{WCA}, which is given by [36]

$$V_{\text{WCA}}(r_{ij})$$
$$= \begin{cases} 4\varepsilon[(\sigma/r_{ij})^{12} - (\sigma/r_{ij})^6] + \varepsilon & r_{ij} \in [0, 2^{1/6}\sigma) \\ 0 & r_{ij} \in [2^{1/6}\sigma, +\infty) \end{cases}, \quad (27)$$

where r_{ij} is the distance between the ith and jth particles, and the parameters ε and σ have dimensions of energy and length, respectively. The WCA potential enables rapid computations of particle interactions due to the short cutoff distance of this potential. The WCA potential is not realistic in the sense
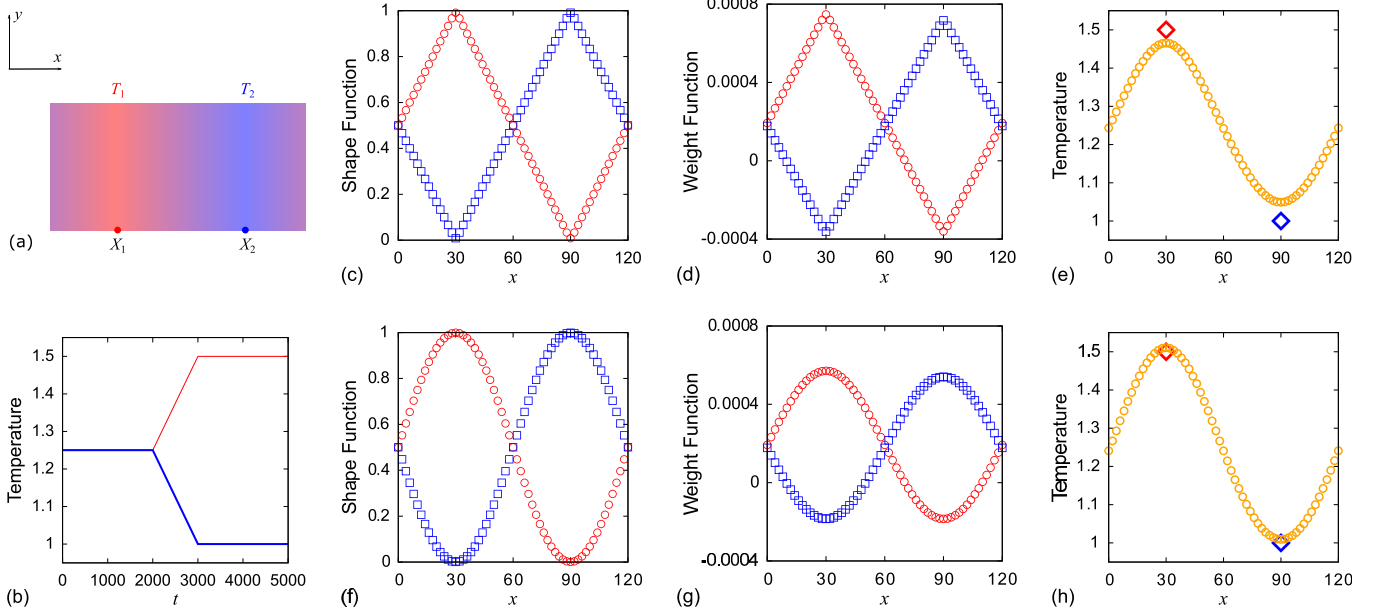
FIG. 2. (a) Schematic of the virtual point configuration and the temperature field for $N_{VP} = 2$. (b) Time evolution of T_1 (thin lines) and T_2 (thick lines). (c–e) The x coordinate dependence of (c) the shape functions, (d) the average weight functions, and (e) the temperature profile (circles) at the nonequilibrium steady state produced using the shape function defined by Eq. (28). (f–h) The x coordinate dependence of (f) the shape functions, (g) the average weight functions, and (h) the temperature profile (circles) at the nonequilibrium steady state produced using the shape function defined by Eq. (29). Circles and squares plotted in panels (c), (d), (f), and (g) signify the values associated with $I = 1$ and 2, respectively. Diamonds plotted in panels (e) and (h) indicate the coarse-grained temperatures.

that this potential is purely repulsive. However, we describe results obtained by adopting this potential here because our main objective in this paper is to verify the validity of the present method. Note that the present method can be applied to systems interacting via other potentials. Some of the results obtained by applying the present method to the system using the Lennard-Jones potential are described in Appendix C.

When the length, mass, and the energy units are defined by σ, m, and ε, respectively, the unit of time is given by $\sigma\sqrt{m/\varepsilon}$. Subsequently, σ, m, and ε are set to 1. Furthermore, k_B is set to 1. The equations of motion are numerically solved by the fourth-order Runge-Kutta method with the coefficients given by Eq. (25), and the time step is set to 0.001.

In general, when the velocities are evolved using the present method, the system's total momentum is not conserved. In the present simulations, we impose the additional constraints to ensure that each component of the velocity of the center of masses remains 0. As shown in Appendix D, these constraints can also be treated using Gauss's principle of least constraint.

A. One-dimensional temperature nonuniformity

Here, we present the case where N_{VP} virtual points for constraining the coarse-grained temperature are set on the line $y = 0$, and the shape function is independent of the y coordinates of the particle positions. Then, the produced nonequilibrium state is homogeneous in the y-direction, and we study the dependence of physical quantities on the x coordinate. We set $(L_x, L_y) = (120, 60)$ and $N = 5400$.

First, we consider the case where $N_{VP} = 2$ and the x coordinates X_I of the virtual points are 30 and 90 for $I = 1$

and 2, respectively. A schematic picture of the virtual point configuration is exhibited in Fig. 2(a). The coarse-grained temperature T_I is controlled as shown in Fig. 2(b), and data for evaluating quantities under a nonequilibrium steady state are collected at t between 4000 and 5000. Furthermore, the error bars displayed in the figures are variances computed from 200 different initial ensembles, and they are omitted if the errors are less than the point size.

In this case, the simplest shape function for the ith particle can be introduced using the piecewise linear function as

$$\mathcal{S}_{iI} = \begin{cases} (x_i - X_{I-1})/(X_I - X_{I-1}) & x_i \in [X_{I-1}, X_I) \\ (X_{I+1} - x_i)/(X_{I+1} - X_I) & x_i \in [X_I, X_{I+1}), \\ 0 & \text{otherwise} \end{cases} \quad (28)$$

where we assume $X_{I \pm N_{VP}} = X_I \pm L_x$. This shape function is plotted in Fig. 2(c), and the average weight function at a nonequilibrium steady state is plotted in Fig. 2(d). The weight function is also piecewise linear, and it takes a negative value at the region distant from the corresponding virtual point. The temperature profile at the nonequilibrium steady state produced using this shape function is shown in Fig. 2(e), where the temperature smoothly varies with the x coordinate even though Eq. (28) gives the linear interpolation of the temperature. The smooth variation of the temperature implies that the constraint using the shape function is not strong. Although qualitative behavior of the temperature is reasonably good, the local temperatures at X_1 and X_2 somewhat deviate from T_1 and T_2, respectively. From the temperature control perspective, it is desirable that the local temperature at X_I equals T_I. Therefore, it is necessary to consider the method for improvement.
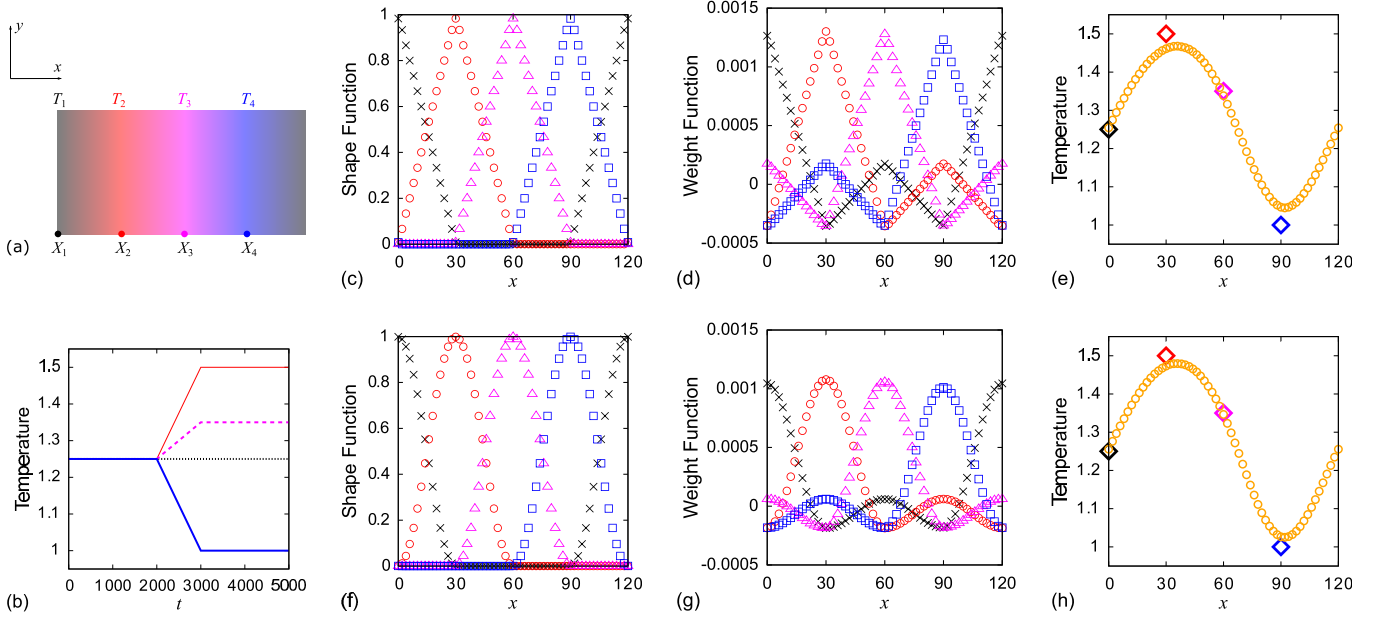
FIG. 3. (a) Schematic of the virtual point configuration and the temperature field for $N_{VP} = 4$. (b) Time evolution of T_1 (dotted lines), T_2 (thin lines), T_3 (dashed lines), and T_4 (thick lines). (c–e) The x coordinate dependence of (c) the shape functions, (d) the average weight functions, and (e) the temperature profile (circles) at the nonequilibrium steady state produced using the shape function defined by Eq. (28). (f–h) The x coordinate dependence of (f) the shape functions, (g) the average weight functions, and (h) the temperature profile (circles) at the nonequilibrium steady state produced using the shape function defined by Eq. (29). Crosses, circles, triangles, and squares plotted in panels (c), (d), (f), and (g) signify the values associated with $I = 1, 2, 3$, and 4, respectively. Damonds plotted in panels (e) and (h) represent the coarse-grained temperatures.

One reason for this deviation is that the shape function is not smooth at X_I as shown in Fig. 2(c). To overcome this drawback, the following shape function is introduced:

$$S_{iI} = \begin{cases} 0.5\{1 + \cos[(X_I - x_i)\pi/(X_I - X_{I-1})]\} & x_i \in [X_{I-1}, X_I) \\ 0.5\{1 - \cos[(X_{I+1} - x_i)\pi/(X_{I+1} - X_I)]\} & x_i \in [X_I, X_{I+1}). \\ 0 & \text{otherwise} \end{cases} \quad (29)$$

This shape function is smooth at X_1 and X_2 as shown in Fig. 2(f). In Fig. 2(g), we plot the average weight function at a nonequilibrium steady state produced using the shape function given by Eq. (29). The weight function is also smooth at X_1 and X_2, and the amplitude of the weight function is suppressed compared to that obtained from the piecewise linear shape function. Moreover, the temperature profile at the nonequilibrium steady state is plotted in Fig. 2(h). Figure 2(h) clearly shows that the deviation of the temperatures at X_1 and X_2 is successfully suppressed.

Second, we consider the case where $N_{VP} = 4$ and X_1, X_2, X_3, and X_4 are set to 0, 30, 60, and 90, respectively. A schematic picture of the virtual point configuration is shown in Fig. 3(a), and the coarse-grained temperatures at X_1, X_2, X_3, and X_4 are controlled as shown in Fig. 3(b). The shape function, average weight function, and the temperature profile at a nonequilibrium steady state produced by this condition with the shape function given by Eq. (28) are shown in Figs. 3(c), 3(d), and 3(e), respectively. The temperatures at X_1 and X_3 are approximately equal to T_1 and T_3, respectively. However, there are temperature deviations at X_2 and X_4, similar to the case for $N_{VP} = 2$. Figures 3(f), 3(g), and 3(h) exhibit the shape function, average weight function, and the temperature profile

at a nonequilibrium steady state produced using the shape function given by Eq. (29), respectively. Though the temperature deviations at X_2 and X_4 from the coarse-grained values are reduced to some degree, there is still scope for further improvement by introducing an appropriate shape function.

To construct the shape function, we assume that the temperature profile is expressed using a piecewise cubic function as

$$T(x) = T_I + \sum_{\nu=1}^{3} h_{I,\nu}(x - X_I)^{\nu} \quad x \in [X_I, X_{I+1}), \quad (30)$$

where $h_{I,\nu}$ is the coefficient determined from conditions imposed at each X_I. Here we set C^2-continuity at every X_I. Then, the coefficients in Eq. (30) are obtained by solving linear equations, which can be written as

$$\mathcal{P}(X_1, \cdots, X_{N_{VP}})\boldsymbol{h} = \boldsymbol{q}, \quad (31)$$

where $\boldsymbol{h} = (h_{1,1}, h_{1,2}, h_{1,3} \cdots, h_{N_{VP},1}, h_{N_{VP},2}, h_{N_{VP},3})^T$, $\boldsymbol{q} = (T_2 - T_1, T_3 - T_2, \cdots, T_{N_{VP}} - T_{N_{VP}-1}, T_1 - T_{N_{VP}}, 0, \cdots, 0)^T$, and $\mathcal{P}(X_1, \cdots, X_{N_{VP}})$ is a $3N_{VP} \times 3N_{VP}$ matrix whose entries are functions of $X_1, \cdots, X_{N_{VP}}$. By solving Eq. (31), $h_{I,\nu}$ is
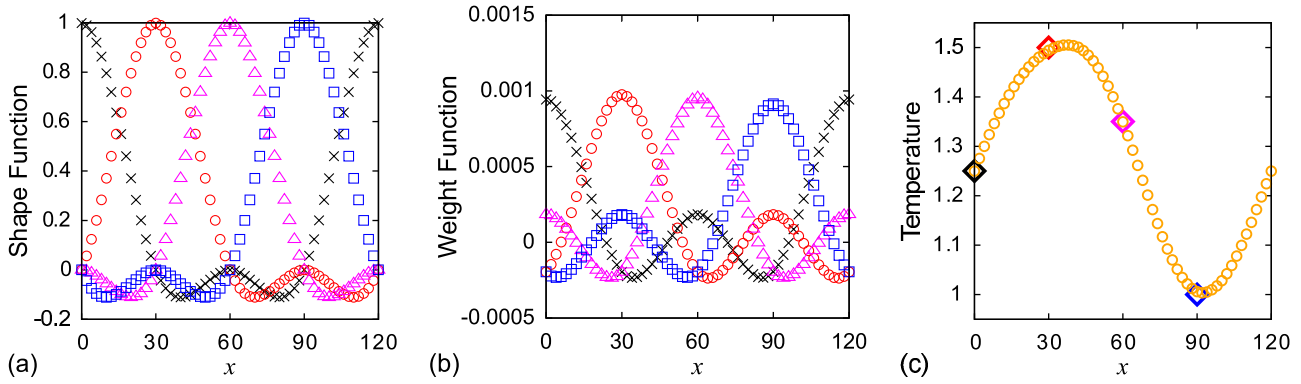
FIG. 4. The x coordinate dependence of (a) the shape functions, (b) the average weight functions, and (c) the temperature profile (circles) at the nonequilibrium steady state produced using the shape function derived from the cubic interpolation. Crosses, circles, triangles, and squares plotted in panels (a) and (b) signify the values associated with $I = 1, 2, 3,$ and 4, respectively. Diamonds plotted in panel (c) indicate the coarse-grained temperatures.

obtained as

$$h_{I,\nu} = \sum_{J=1}^{N_{\mathrm{VP}}} \mathcal{P}^{-1}_{(3I+\nu,J)} (T_{J+1} - T_J),\qquad(32)$$

where $T_{J+N_{\mathrm{VP}}} = T_J$ from the periodic boundary condition and $\mathcal{P}^{-1}_{(\alpha,\beta)}$ denotes the (α, β) entry of $\mathcal{P}^{-1}$. Substituting Eq. (32) into Eq. (30), it is easily shown that $T(x)$ is written in the form

$$T(x) = \sum_{I=1}^{N_{\mathrm{VP}}} s_I(x)T_I, \quad \sum_{I=1}^{N_{\mathrm{VP}}} s_I(x) = 1.\qquad(33)$$

As a result, the temperature profile defined by Eq. (30) can be expressed in the form given by Eq. (1). We can use $s_I(x)$ as the shape function if we assume the interpolation given by Eq. (30).

When the shape function derived from Eq. (30) is applied to the case shown in Fig. 3, the shape function can be plotted as shown in Fig. 4(a). The shape function does not vanish even in regions far from the virtual points. In addition, the shape function can have a negative value. These properties do not appear for the shape functions defined by Eqs. (28) and (29). Figure 4(b) depicts the average weight function at a nonequilibrium steady state produced by the shape function derived from Eq. (30). The feature of the weight function is similar to that obtained from the shape function given by Eq. (29). The temperature profile at this nonequilibrium steady state is shown in Fig. 4(c). The temperature deviation from the coarse-grained value is sufficiently small for every X_I. As a result, we can conclude that the shape function defined here outperforms those obtained by Eqs. (28) and (29).

Furthermore, we investigate the properties of the nonequilibrium steady state produced by the shape function derived from Eq. (30). First, we consider the distribution of the velocity $\dot{\boldsymbol{r}} = (v_x, v_y)$. The heat maps in Figs. 5(a) and 5(b) show the dependence of v_x and v_y probability densities on the x coordinate, respectively. There is no discernible difference between the v_x and v_y distributions: In the colder region, the peak at $v = 0$ is high and narrow, while in the hotter region, it becomes low and broad. The distributions of v_x at X_1 and X_2 are plotted in Fig. 5(c) and those at X_3 and X_4 in Fig. 5(d). The curves in Figs. 5(c) and 5(d) are obtained by

fitting Maxwell's distribution function to the simulation data. The optimal temperatures of Maxwell's distribution function at X_1, X_2, X_3, and X_4 obtained through this fitting procedure are 1.25126, 1.49556, 1.35115, and 1.00699, respectively. Figures 5(c) and 5(d) exhibit that Maxwell's distribution function can successfully represent the velocity distributions with temperatures very close to the coarse-grained values. This result implies that the produced nonequilibrium steady state may be regarded as a local equilibrium state.

In Fig. 6(a), the density profile is shown, where density decreases in the hotter region, while it increases in the colder region. This result is intuitively plausible because the pressure
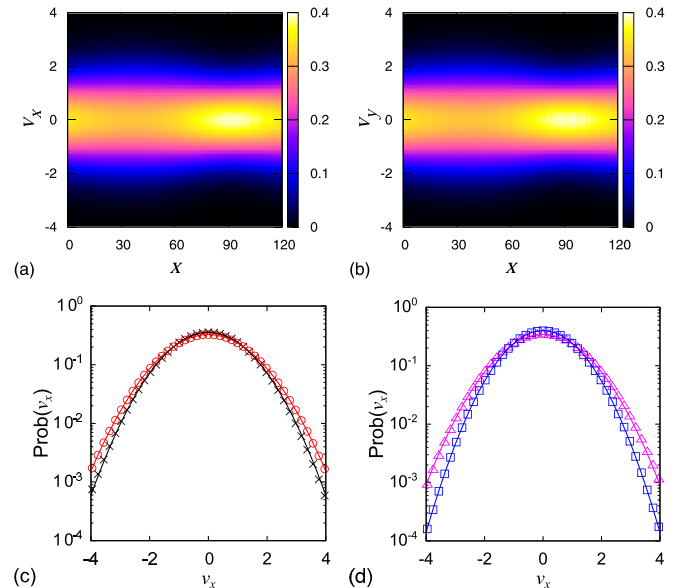
FIG. 5. The velocity distributions when the shape function derived from the cubic interpolation is adopted. (a) The x coordinate dependence of the distribution of v_x. (b) The x coordinate dependence of the distribution of v_y. (c) The distribution of v_x at X_1 (crosses) and X_2 (circles). (d) The distribution of v_x at X_3 (triangles) and X_4 (squares). In panels (c) and (d), the curves are Maxwell's distribution function with the temperature obtained via the fitting procedure.
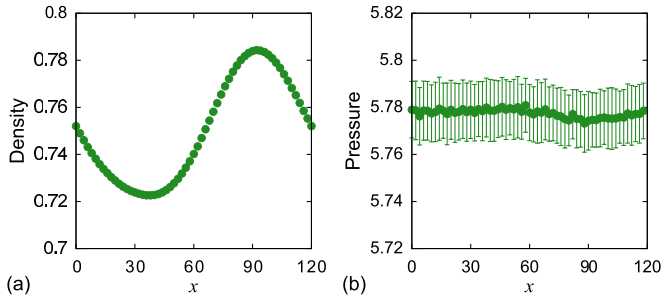
FIG. 6. (a) The density profile and (b) the pressure in the x direction at the nonequilibrium steady state produced using the shape function derived from the cubic interpolation.

gradient in the x direction induced by the temperature nonuniformity is suppressed by the pressure gradient due to density. As shown in Fig. 6(b), the local pressure is nearly constant throughout the entire region. The system maintains the fluid state over the entire region since the density is sufficiently less than that necessary for freezing, even for the colder region [50].

Moreover, the heat flux along the x-direction is depicted in Fig. 7(a). The heat flux exhibits natural behavior, as shown in Figs. 4(c) and 7(a), with heat flowing from the hotter region to the colder region. The heat flux j_Q is written as $j_Q = -\lambda_Q \nabla T$, if the heat is conducted in the system according to Fourier's law, where λ_Q is the thermal conductivity. The relation between the temperature gradient and the heat flux is plotted in Fig. 7(b). This figure clearly demonstrates that the heat flux is strongly correlated with the temperature gradient. In addition, this relationship can be well expressed by a linear function, meaning that the thermal conductivity is nearly constant across the entire region.

In the present method, all particles in the system are subjected to the force to satisfy the constraint conditions. The work done by this constraint force corresponds to the heat received by the system from an external environment. Figure 8(a) shows the x coordinate dependence on the heat received from the external environment per unit time. The system receives heat in the hotter region and releases it in the colder region. However, the behavior of received heat differs from that of the temperature profile. The received heat is large at $x \in [45, 60]$ though temperature drops in this region. A
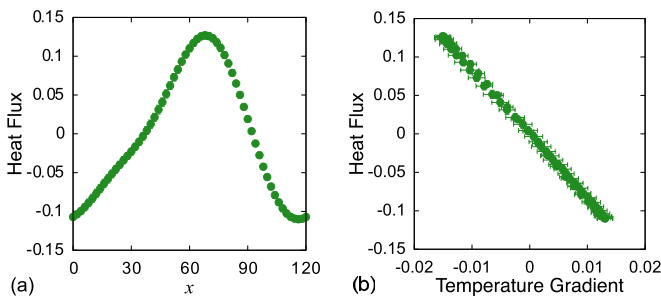
FIG. 7. (a) The x coordinate dependence of the heat flux at the nonequilibrium steady state produced using the shape function derived from the cubic interpolation. (b) Relationship between the temperature gradient and the heat flux.
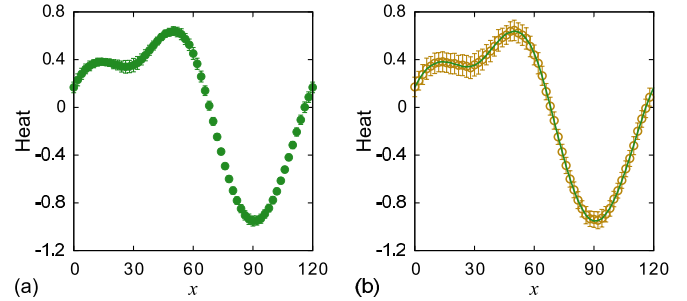
FIG. 8. (a) The x coordinate dependence of the heat per unit time received from the external environment as the work done by the constraint force. (b) The x coordinate dependence of the local heat loss due to the heat flux in the system (circles). The curve displays the result plotted in panel (a).

constraint to maintain the coarse-grained temperature at $x = 60$ to 1.35 is applied in this simulation. If this constraint is not present, then the temperature at $x = 60$ is roughly estimated to be 1.25, i.e., the mean value of the coarse-grained temperatures at X_2 and X_4. As a result of the additional constraint, the region at $x \in [45, 60]$ becomes hotter than in the natural state. Then, excess heat is delivered from the environment to maintain this unnatural state, which is why the received heat becomes so large at $x \in [45, 60]$.

The heat delivered from the environment at a local region is conducted to the neighbor region via the heat flux, and the local heat loss due to the heat flux in the system per unit time is shown in Fig. 8(b). We found that this quantity is equal to the heat received from the environment. That is, the balanced condition for heat is well satisfied locally, suggesting that the system has reached a stationary state and that the data have been collected for a sufficient time.

B. Two-dimensional temperature nonuniformity

Here, we look at the case where four virtual points in the two-dimensional space are used to constrain the coarse-grained temperature. The coordinate of the Ith virtual point is denoted by $\boldsymbol{R}_I = (X_I, Y_I)$. Below, we set $(L_x, L_y) = (120, 120)$ and $(X_I, Y_I) = (60, 0)$, $(60, 60)$, $(0, 60)$, and $(0, 0)$ for $I = 1, 2, 3$, and 4, respectively. The system contains 10800 particles to satisfy the condition that the average number density equals 0.75. The coarse-grained temperature control is conducted according to the same procedure shown in Fig. 3(b), and the data collection approach is the same as in the previous case.

First, the region is divided into triangles, vertices of which correspond to virtual points. The shape function is defined by the coefficients used to express a point's coordinate inside the triangle as a linear combination of the triangle's vertices. The approach for dividing the region into triangles is not unique. For example, the region can be decomposed, as illustrated in Figs. 9(a) and 9(b). For the cases of Figs. 9(a) and 9(b), the shape functions associated with $I = 2$ are presented in Figs. 10(a) and 10(b), respectively. The average weight functions associated with $I = 2$ at a nonequilibrium steady state for the cases illustrated in Figs. 9(a) and 9(b) are shown in Figs. 10(c) and 10(d), respectively. The decomposition
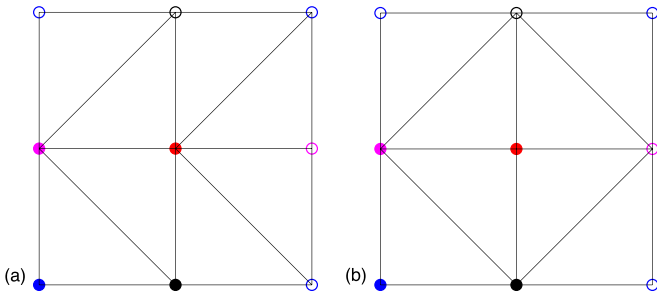
FIG. 9. Examples of decomposition of the simulation cell into triangles. Black, red, magenta, and blue solid circles represent R_1, R_2, R_3, and R_4, respectively. Open circles symbolize periodic copies of the virtual points.

method choice has a significant impact on the shape and weight functions.

When decomposition is performed as illustrated in Figs. 9(a) and 9(b), the temperature profiles at the nonequilibrium steady states are given in Figs. 11(a) and 11(b), respectively. Decomposition method dependence is exhibited by the temperature profiles as well as the shape and weight functions. The temperature profile should be symmetric with respect to lines $x = 60$ and $y = 60$, considering the virtual point configuration and periodic boundary condition. However, Fig. 11(a) confirms that the temperature profile is not symmetric with respect to line $x = 60$, whereas Fig. 11(b) shows that it is symmetric. In particular, the maximum temperature deviates

from R_2 for Fig. 11(a). For the cases shown in Figs. 11(a) and 11(b), the temperature behavior along the lines from R_1 to R_2, R_2 to R_3, R_3 to R_4, and R_4 to R_1 is plotted in Figs. 11(c) and 11(d), respectively. Temperature deviations from the coarse-grained values exist at R_2 and R_4 in both cases. Therefore, it is inappropriate to use linear interpolation with triangle decomposition to produce a nonequilibrium state.

Second, the region is divided into rectangles, the vertices of which correspond to the virtual points. It is assumed that the temperature inside a rectangle is expressed using interpolation as follows:

$$T(\boldsymbol{r}) = \sum_{\mu=0}^{\kappa} \sum_{\nu=0}^{\kappa} h_{I,\mu\nu}(x - X_I)^\mu (y - Y_I)^\nu \quad \boldsymbol{r} \in \Omega_I, \quad (34)$$

where Ω_I represents a rectangular region defined by $[60, 120) \times [0, 60)$, $[60, 120) \times [60, 120)$, $[0, 60) \times [60, 120)$, and $[0, 60) \times [0, 60)$ for $I = 1, 2, 3$ and 4, respectively, and $\boldsymbol{r} = (x, y)$ denotes a coordinate of the point inside Ω_I. Note that $T_I = T(\boldsymbol{R}_I) = h_{I,00}$. Now, consider the cases where κ in Eq. (34) equals 1 and 3, i.e., bilinear and bicubic interpolations. When using the bicubic interpolation, the values of $\partial T/\partial x$, $\partial T/\partial y$, and $\partial^2 T/\partial x \partial y$ at each vertex are required to obtain the coefficients in Eq. (34). We set these values to 0 in this case. The virtual point symmetry supports this choice. The temperature in the entire region can be written in the form given by Eq. (1) using this interpolation. This is proven in the same way that the one-dimensional cubic interpolation was demonstrated above.
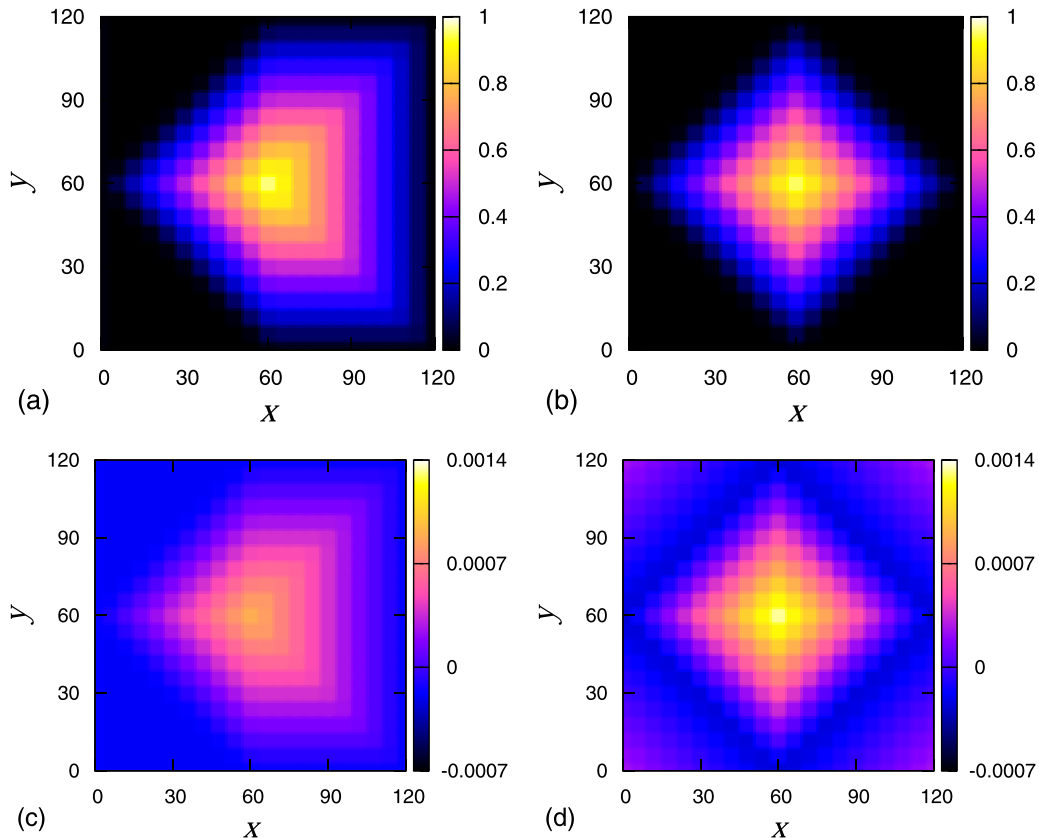
FIG. 10. (a, b) The shape functions associated with $I = 2$ for cases depicted in (a) Fig. 9(a) and (b) Fig. 9(b). (c, d) The average weight functions associated with $I = 2$ for cases depicted in (c) Fig. 9(a) and (d) Fig. 9(b).
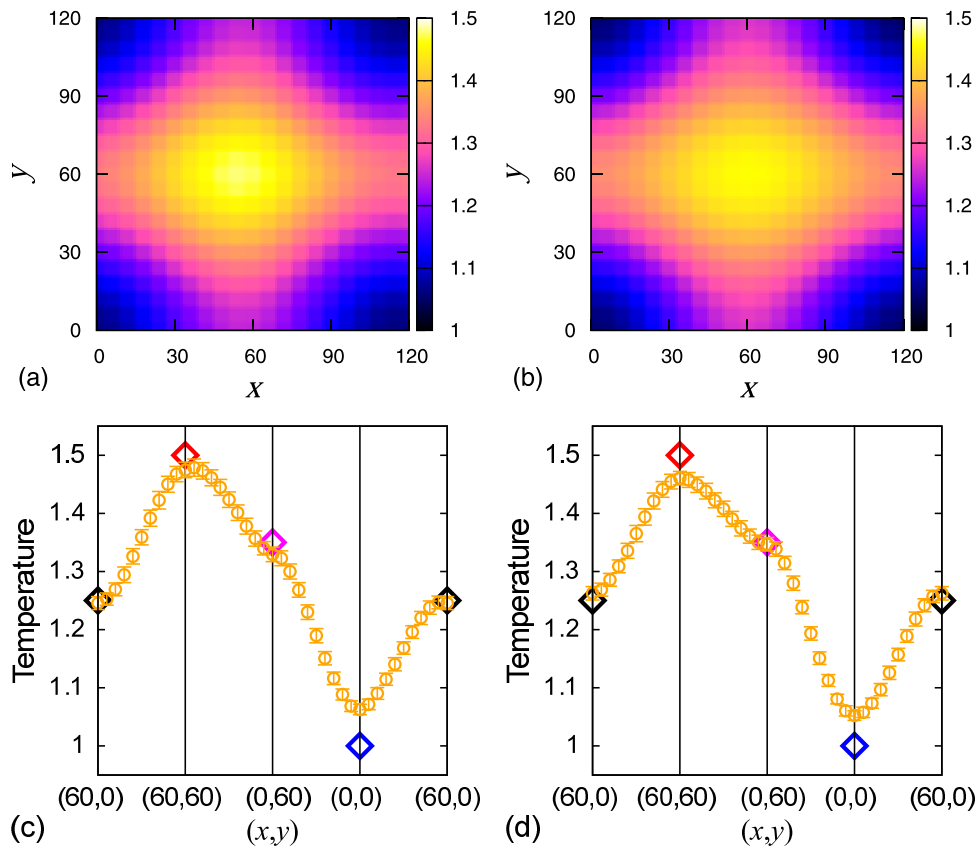
FIG. 11. (a, b) The temperature profile in the xy plane at the nonequilibrium steady state for cases depicted in (a) Fig. 9(a) and (b) Fig. 9(b). (c, d) The temperature along the lines from R_1 to R_2, R_2 to R_3, R_3 to R_4, and R_4 to R_1, for cases depicted in (c) Fig. 9(a) and (d) Fig. 9(b).
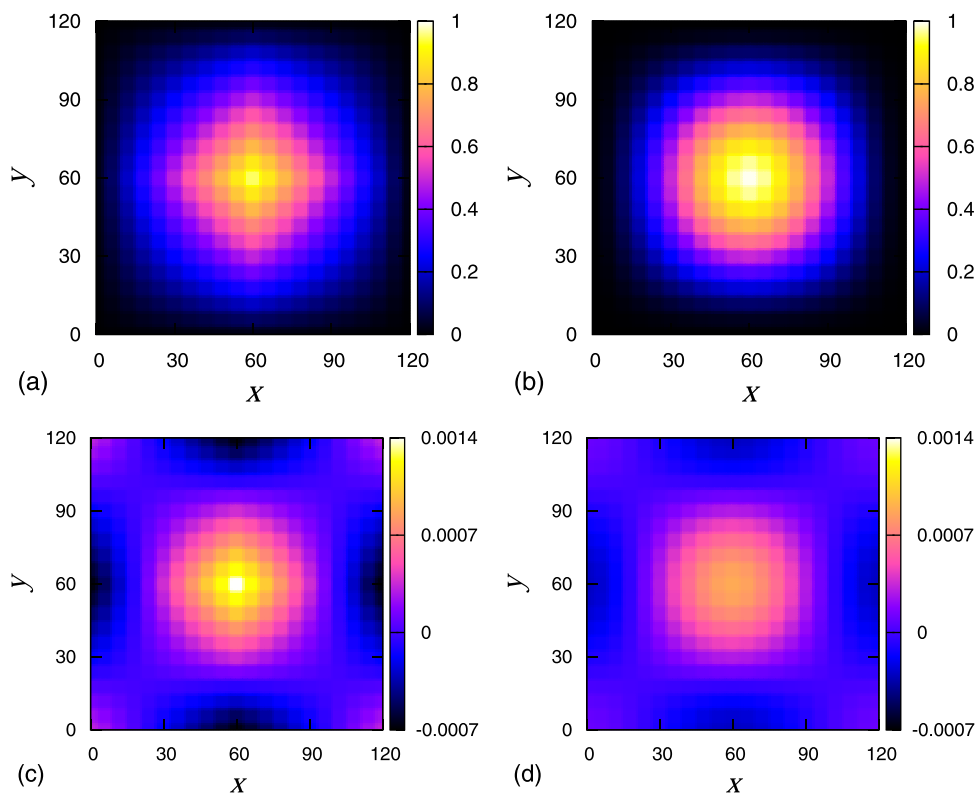
FIG. 12. (a, b) The shape functions associated with $I = 2$ obtained using (a) bilinear and (b) bicubic interpolations. (c, d) The average weight functions associated with $I = 2$ for (c) bilinear and (d) bicubic interpolations.
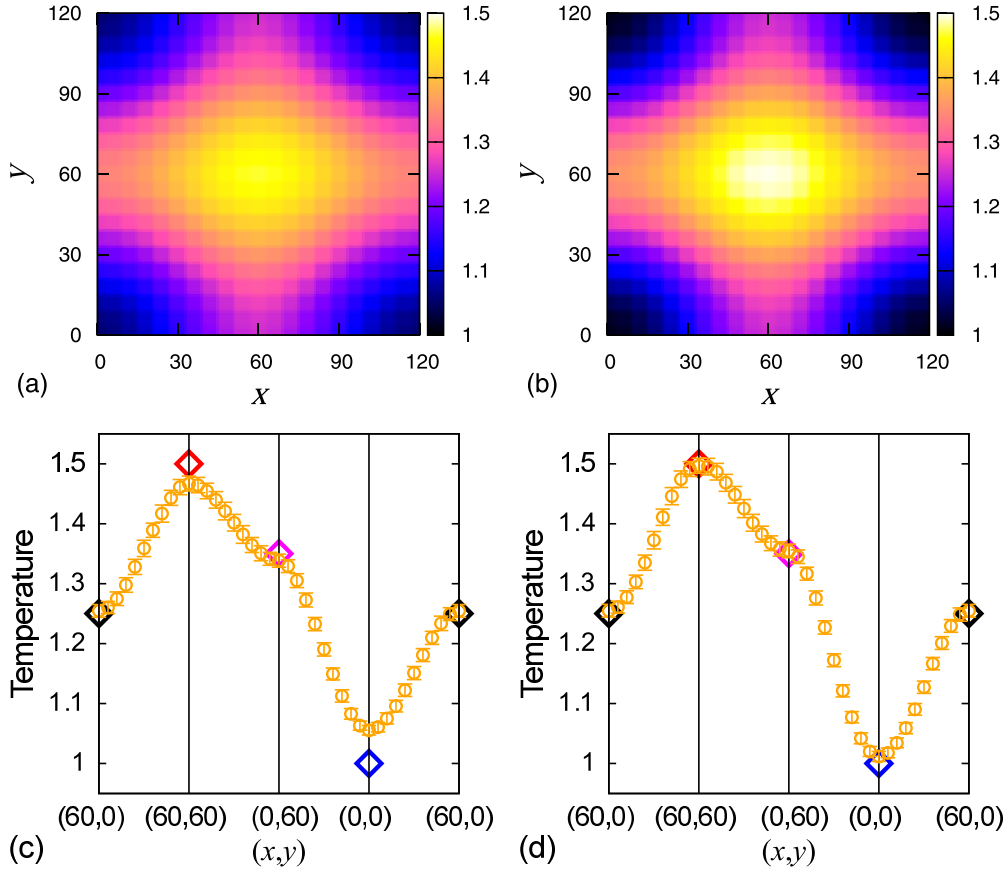
FIG. 13. (a, b) The temperature profile in the *xy* plane at the nonequilibrium steady state for (a) bilinear and (b) bicubic interpolations. (c, d) The temperature along lines from R_1 to R_2, R_2 to R_3, R_3 to R_4, and R_4 to R_1, for (c) bilinear and (d) bicubic interpolations.

Figures 12(a) and 12(b) display the shape functions associated with $I = 2$ for the bilinear and bicubic interpolations, respectively. In both cases, the shape function has a nonnegative value. Figures 12(c) and 12(d) show the average weight functions associated with $I = 2$ at nonequilibrium steady states produced by the bilinear and bicubic interpolations, respectively. Both weight functions have a similar shape, but the variation in the weight function for the bilinear interpolation is greater than the bicubic interpolation. Moreover, Figs. 13(a) and 13(b) illustrate temperature profiles at the nonequilibrium steady states produced using the bilinear and bicubic interpolations, respectively. For the bilinear and bicubic interpolations, the temperature profiles along the same route used to obtain Fig. 11(c) are plotted in Figs. 13(c) and 13(d), respectively. There is still a temperature deviation from the coarse-grained values at R_2 and R_4 in the case of the bilinear interpolation. These deviations are comparable to those observed when using the linear interpolation with the triangle decomposition. However, when the bicubic interpolation is employed, these deviations are relatively small for all I. As a result, it is concluded that the desired temperature profile can be obtained using the shape function constructed by the bicubic interpolation.

IV. CONCLUSION

In this paper, we proposed a method for producing a nonequilibrium state by constraining coarse-grained physical quantities at virtual points set in a system using Gauss's principle of least constraint. In this formulation, we define a rule for interpolating the physical quantities at any point in the system from those at the virtual points in advance. The shape function matrix is constructed according to this rule when computing the coarse-grained physical quantities. Then, the weight function matrix, which enables the calculation of the coarse-grained physical quantities at the virtual points from the microscopic quantities, is obtained as a Moore-Penrose pseudoinverse matrix of the shape function matrix. These matrices are used to construct linear equations for the Lagrange multipliers of the constraints. The constraint forces are calculated using the Lagrange multipliers, which are obtained by solving these equations.

The proposed method was applied to constraints on the coarse-grained kinetic energies at the virtual points. A nonuniform temperature field is produced by constraining them to different values according to the virtual points. We discovered that the temperature field at a nonequilibrium steady state is dependent on the interpolation rule. When linear interpolation is adopted for this rule, there is a nonnegligible difference between the coarse-grained and local temperatures. We showed that this difference was considerably reduced by adopting cubic interpolation to construct the shape function matrix. The reduction in this difference facilitates obtaining desirable nonequilibrium states.

In principle, the present method is applicable to other physical quantities as well as the case where multiple

physical quantities are controlled. As stated in the introduction, fluid flow is one essential application of nonequilibrium MD. The present method is applicable by constraining the coarse-grained momentum to produce particle flow. Further applications of the present method will be reported in the future. In addition, it is possible to simulate a more realistic situation by incorporating an appropriate fluctuation in the control of the coarse-grained physical quantities. Therefore, it is worth addressing further improvement of the methodology, including this issue.

APPENDIX A: MOORE-PENROSE PSEUDOINVERSE MATRIX FOR MINIMIZING THE MEAN SQUARED ERROR OF ESTIMATED PHYSICAL QUANTITY

When the microscopic physical quantity $\boldsymbol{a}$ is given, the coarse-grained physical quantity $\boldsymbol{A}$ is calculated by Eq. (3). Then, the microscopic physical quantity can be expressed using $\boldsymbol{A}$ through Eq. (2), and this is denoted by $\tilde{\boldsymbol{a}}$. Here, we consider the mean squared error between $\boldsymbol{a}$ and $\tilde{\boldsymbol{a}}$, which is given by

$$g(\mathcal{W}) = \frac{1}{N}(\tilde{\boldsymbol{a}}(\mathcal{W}) - \boldsymbol{a})^T(\tilde{\boldsymbol{a}}(\mathcal{W}) - \boldsymbol{a})$$
$$= \frac{1}{N}(\mathcal{SW}\boldsymbol{a} - \boldsymbol{a})^T(\mathcal{SW}\boldsymbol{a} - \boldsymbol{a}). \quad \text{(A1)}$$

The derivative of $g(\mathcal{W})$ with respect to $\mathcal{W}_{\alpha\beta}$ is calculated as

$$\frac{\partial g(\mathcal{W})}{\partial \mathcal{W}_{\alpha\beta}} = \frac{1}{N}\left[\left(\mathcal{S}\frac{\partial \mathcal{W}}{\partial \mathcal{W}_{\alpha\beta}}\boldsymbol{a}\right)^T(\mathcal{SW}\boldsymbol{a} - \boldsymbol{a})\right.$$
$$\left. + (\mathcal{SW}\boldsymbol{a} - \boldsymbol{a})^T\left(\mathcal{S}\frac{\partial \mathcal{W}}{\partial \mathcal{W}_{\alpha\beta}}\boldsymbol{a}\right)\right]$$
$$= \frac{1}{N}[(a_\beta \mathcal{S}\boldsymbol{e}_\alpha)^T(\mathcal{SW}\boldsymbol{a} - \boldsymbol{a}) + (\mathcal{SW}\boldsymbol{a} - \boldsymbol{a})^T(a_\beta \mathcal{S}\boldsymbol{e}_\alpha)]$$
$$= \frac{1}{N}a_\beta\{\boldsymbol{e}_\alpha^T(\mathcal{S}^T\mathcal{SW} - \mathcal{S}^T)\boldsymbol{a}$$
$$+ [\boldsymbol{e}_\alpha^T(\mathcal{S}^T\mathcal{SW} - \mathcal{S}^T)\boldsymbol{a}]^T\}$$
$$= \frac{2}{N}a_\beta \boldsymbol{e}_\alpha^T(\mathcal{S}^T\mathcal{SW} - \mathcal{S}^T)\boldsymbol{a}, \quad \text{(A2)}$$

where a_β is the βth component of $\boldsymbol{a}$, $\boldsymbol{e}_\alpha$ is the vector whose ηth component is $\delta_{\alpha\eta}$. It is confirmed that Eq. (A2) is 0 irrespective of $\boldsymbol{a}$ when Eq. (6) is adopted as $\mathcal{W}$.

Since $g(\mathcal{W})$ is a quadratic function of entries of $\mathcal{W}$, Eq. (A1) can be written as

$$g(\mathcal{W}) = g(\mathcal{W}^*) + \frac{1}{2}\sum_\alpha\sum_\beta\sum_\mu\sum_\nu \frac{\partial^2 g}{\partial \mathcal{W}_{\alpha\beta}\partial \mathcal{W}_{\mu\nu}}$$
$$\times (\mathcal{W}_{\alpha\beta} - \mathcal{W}_{\alpha\beta}^*)(\mathcal{W}_{\mu\nu} - \mathcal{W}_{\mu\nu}^*), \quad \text{(A3)}$$

where $\mathcal{W}^*$ represents the stationary point of g. The second derivative of $g(\mathcal{W})$ is computed as

$$\frac{\partial^2 g}{\partial \mathcal{W}_{\alpha\beta}\partial \mathcal{W}_{\mu\nu}} = \frac{2a_\beta}{N}\boldsymbol{e}_\alpha^T\mathcal{S}^T\mathcal{S}\left(\frac{\partial \mathcal{W}}{\partial \mathcal{W}_{\mu\nu}}\right)\boldsymbol{a}$$
$$= \frac{2a_\beta a_\nu}{N}(\mathcal{S}\boldsymbol{e}_\alpha)^T\mathcal{S}\boldsymbol{e}_\mu. \quad \text{(A4)}$$

Then, the second term on the right-hand side in Eq. (A3) is calculated as

$$\frac{1}{2}\sum_\alpha\sum_\beta\sum_\mu\sum_\nu \frac{\partial^2 g}{\partial \mathcal{W}_{\alpha\beta}\partial \mathcal{W}_{\mu\nu}}(\mathcal{W}_{\alpha\beta} - \mathcal{W}_{\alpha\beta}^*)(\mathcal{W}_{\mu\nu} - \mathcal{W}_{\mu\nu}^*)$$

$$= \frac{1}{N}\sum_\alpha\sum_\beta\sum_\mu\sum_\nu a_\beta a_\nu(\mathcal{W}_{\alpha\beta} - \mathcal{W}_{\alpha\beta}^*)(\mathcal{W}_{\mu\nu} - \mathcal{W}_{\mu\nu}^*)(\mathcal{S}\boldsymbol{e}_\alpha)^T\mathcal{S}\boldsymbol{e}_\mu$$

$$= \frac{1}{N}\left[\sum_\alpha\sum_\beta a_\beta(\mathcal{W}_{\alpha\beta} - \mathcal{W}_{\alpha\beta}^*)\mathcal{S}\boldsymbol{e}_\alpha\right]^T\left[\sum_\alpha\sum_\beta a_\beta(\mathcal{W}_{\alpha\beta} - \mathcal{W}_{\alpha\beta}^*)\mathcal{S}\boldsymbol{e}_\alpha\right]. \quad \text{(A5)}$$

Eq. (A5) shows that the second term on the right-hand side in Eq. (A3) is not negative irrespective of $\boldsymbol{a}$. Therefore, Eq. (6) gives the minimum value of Eq. (A1).

APPENDIX B: SYSTEMATIC DRIFT OF TEMPERATURE

We consider the case where $N_{\text{VP}} = 2$ and the shape function is given by Eq. (28). The initial configurations and

velocities are taken from the results at $t = 4000$ used to obtain Figs. 2(c)–2(e). The simulation is conducted with maintaining the coarse-grained temperature at its initial value, but $\partial T_I/\partial t$ in Eq. (18) is set to 0 instead of using the adaptive correction given by Eq. (26). Time evolutions of the coarse-grained temperatures at X_1 and X_2 obtained by adopting the velocity Verlet method are shown in Figs. 14(a) and 14(b), respectively. Here, the fixed-point iteration method is applied
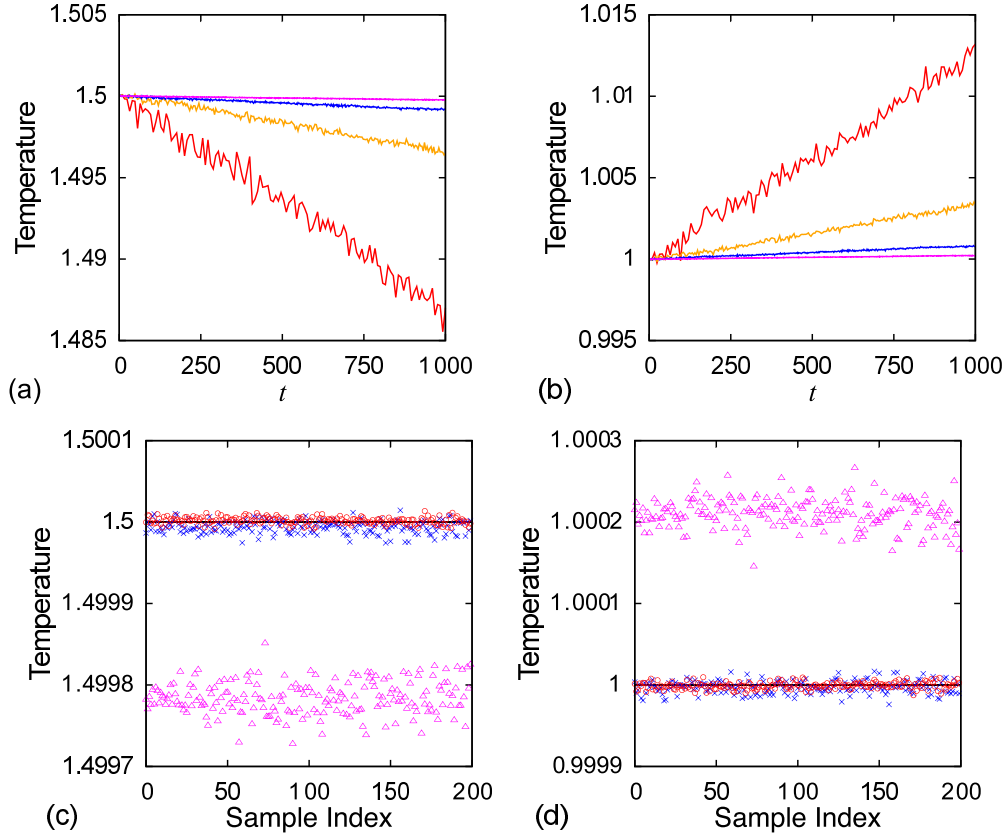
FIG. 14. (a) Time evolution of the coarse-grained temperature at X_1 by adopting the velocity Verlet method. $\delta t = 0.001, 0.002, 0.004,$ and 0.008 from the top. (b) Time evolution of the coarse-grained temperature at X_2 by adopting the velocity Verlet method. $\delta t = 0.001, 0.002,$ 0.004, and 0.008 from the bottom. (c) The coarse-grained temperatures of 200 samples at X_1 for $t = 1000$. (d) The coarse-grained temperatures of 200 samples at X_2 for $t = 1000$. In panels (c) and (d), triangles, crosses, and circles are obtained by employing the velocity Verlet method, the conventional fourth-order Runge-Kutta method, and the fourth-order Runge-Kutta method with the 3/8-rule, respectively.

to solve the self-consistent equation mentioned in Sec. II D until the velocity variation of all particles is less than 10^{-12}. In this case, four iterations are typically required to satisfy this condition. The coarse-grained temperatures at X_1 and X_2 deviate from their initial values, i.e., 1.5 at X_1 and 1.0 at X_2, though it is sufficiently small for $\delta t = 0.001$. Additionally, the deviation and fluctuation in the coarse-grained temperature increase as δt increases.

The coarse-grained temperatures at X_1 and X_2 for $t = 1000$ obtained from 200 samples with $\delta t = 0.001$ are plotted in Figs. 14(c) and 14(d), respectively. We compare three schemes for numerical integration of the equations of motion: The velocity Verlet method, the conventional fourth-order

Runge-Kutta method [the coefficients given by Eq. (24)], and the fourth-order Runge-Kutta method with the 3/8-rule [the coefficients given by Eq. (25)]. Figure 14 clearly shows that the coarse-grained temperature systematically deviates from the designated value when the velocity Verlet method is adopted. However, the coarse-grained temperature obtained from the fourth-order Runge-Kutta method fluctuates around the designated value. By comparing two fourth-order Runge-Kutta methods, it is found that the magnitudes of the deviations for the fourth-order Runge-Kutta method with the 3/8-rule are less than those for the conventional Runge-Kutta method, i.e., the former method gives more stable results. That is, we can say that the fourth-order Runge-Kutta method

TABLE I. Deviation of the coarse-grained temperature at X_1.

δt	Velocity Verlet	Runge-Kutta	Runge-Kutta 3/8-rule
0.0005	$-5.40 \times 10^{-5} \pm 7.44 \times 10^{-6}$	$5.97 \times 10^{-8} \pm 3.60 \times 10^{-6}$	$1.59 \times 10^{-8} \pm 2.26 \times 10^{-6}$
0.001	$-2.16 \times 10^{-4} \pm 2.02 \times 10^{-5}$	$-6.35 \times 10^{-6} \pm 7.76 \times 10^{-6}$	$1.92 \times 10^{-6} \pm 4.35 \times 10^{-6}$
0.002	$-8.61 \times 10^{-4} \pm 6.31 \times 10^{-5}$	$-2.03 \times 10^{-4} \pm 1.58 \times 10^{-5}$	$6.03 \times 10^{-5} \pm 9.06 \times 10^{-6}$
0.004	$-3.42 \times 10^{-3} \pm 2.26 \times 10^{-4}$	$-6.60 \times 10^{-3} \pm 3.13 \times 10^{-5}$	$1.36 \times 10^{-3} \pm 2.29 \times 10^{-5}$
0.008	$-1.36 \times 10^{-2} \pm 8.15 \times 10^{-4}$	$-1.82 \times 10^{-1} \pm 2.75 \times 10^{-4}$	$-3.80 \times 10^{-2} \pm 1.93 \times 10^{-4}$

TABLE II. Deviation of the coarse-grained temperature at X_2.

δt	Velocity Verlet	Runge-Kutta	Runge-Kutta (3/8-rule)
0.0005	$5.26 \times 10^{-5} \pm 7.49 \times 10^{-6}$	$-3.25 \times 10^{-7} \pm 3.64 \times 10^{-6}$	$-1.74 \times 10^{-8} \pm 2.28 \times 10^{-6}$
0.001	$2.11 \times 10^{-4} \pm 1.80 \times 10^{-5}$	$-2.61 \times 10^{-6} \pm 7.82 \times 10^{-6}$	$-7.83 \times 10^{-7} \pm 4.39 \times 10^{-6}$
0.002	$8.41 \times 10^{-4} \pm 5.43 \times 10^{-5}$	$-9.40 \times 10^{-5} \pm 1.61 \times 10^{-5}$	$-1.57 \times 10^{-5} \pm 9.19 \times 10^{-6}$
0.004	$3.33 \times 10^{-3} \pm 1.89 \times 10^{-4}$	$-3.11 \times 10^{-3} \pm 3.04 \times 10^{-5}$	$-5.70 \times 10^{-4} \pm 2.11 \times 10^{-5}$
0.008	$1.31 \times 10^{-2} \pm 6.75 \times 10^{-4}$	$-8.85 \times 10^{-2} \pm 1.93 \times 10^{-4}$	$-3.36 \times 10^{-2} \pm 1.38 \times 10^{-4}$

with the 3/8-rule is suitable for numerical integration of the equations of motion with $\delta t = 0.001$.

Tables I and II establish that the coarse-grained temperature's deviation depends on the time step and the numerical integration method. The fourth-order Runge-Kutta method with the 3/8-rule is superior to the velocity Verlet method for $\delta t \leqslant 0.004$. Although the deviation produced by the velocity Verlet method is smaller than that by the fourth-order Runge-Kutta method for $\delta t = 0.008$, it is not appropriate to apply the present method without a correction for this time step. The numerical integration scheme characteristics also appear through the deviation tendencies when the time step increases. For the velocity Verlet method, the coarse-grained temperature gradually approaches with the increase in the time step.

However, both coarse-grained temperatures decrease for the conventional fourth-order Runge-Kutta method.

APPENDIX C: NONEQUILIBRIUM STEADY STATE OF LENNARD-JONES SYSTEM

We consider the system whose particles interact via the Lennard-Jones (LJ) potential $V_{LJ}(r_{ij}) = 4\varepsilon[(\sigma/r_{ij})^{12} - (\sigma/r_{ij})^{6}]$. The cutoff distance of the potential is set to 3σ. We apply the present method with conditions used to obtain the results displayed in Fig. 4 to this system. Then, the x coordinate dependence of physical quantities can be obtained as shown in Fig. 15. The temperature profile for the LJ system
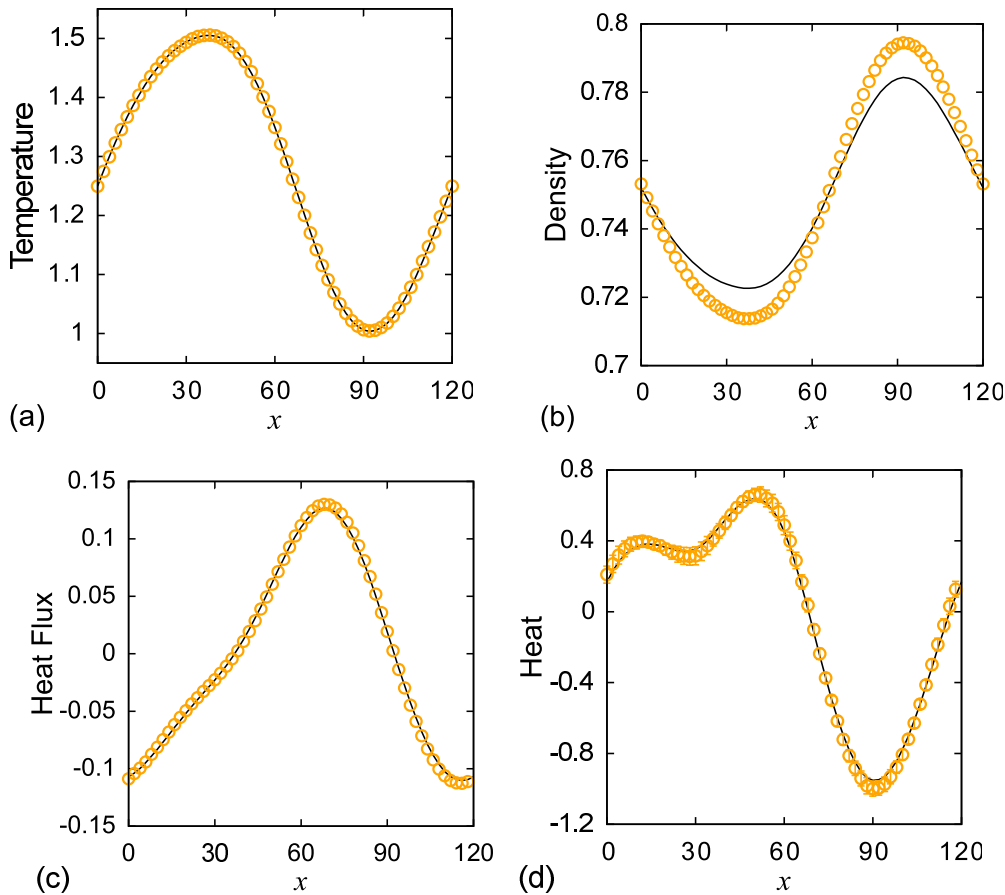
FIG. 15. The x coordinate dependence of the physical quantities for the Lennard-Jones system under the nonequilibrium steady state. (a) Temperature, (b) density, (c) heat flux, and (d) heat received from the external environment. Curves plotted in figures are results for the WCA system.

shown in Fig. 15(a) is not distinguishable from that for the WCA system. That is, the present method is successfully applied to the LJ system. The difference between the LJ and WCA systems can noticeably be seen in the density profile, as shown in Fig. 15(b). The density variation becomes large for the LJ system, and the pressure of the LJ system is about 3.57, which is lower than the WCA system due to the attractive interaction. The properties related to the heat are exhibited in Figs. 15(c) and 15(d). Figure 15(c) presents the heat flux in the system, while Fig. 15(d) shows the heat received from the external environment. Evidently, the difference between the LJ and WCA systems is sufficiently small for both quantities because the heat is mainly conducted via particle collisions in high-density fluid. Thus, the repulsive component of the potential plays a crucial role in thermal conductivity. Notably, Ishii *et al.* demonstrated that the thermal conductivity obtained by the LJ potential for the three-dimensional system is approximately equal to the WCA potential when the conditions are the same, except the cutoff distance [51].

APPENDIX D: APPLICATION OF GAUSS'S PRINCIPLE OF LEAST CONSTRAINT TO THE VELOCITY OF THE CENTER OF MASSES

The constraint condition for the velocity of the center of masses of the entire system is written as

$$B_\alpha = \sum_{i=1}^{N} m_i \dot{r}_{i,\alpha} - V_\alpha(t) = 0, \tag{D1}$$

where $V_\alpha(t)$ is the value of the αth component of the velocity of the center of masses at time t. By differentiating Eq. (D1) with respect to time, we obtain

$$\sum_{i=1}^{N} m_i \ddot{r}_{i,\alpha} - \frac{dV_\alpha}{dt} = 0. \tag{D2}$$

Since Eq. (D2) has the same form as Eq. (8), i.e., $\boldsymbol{b}_{\alpha,i} = m_i \boldsymbol{e}_\alpha$ and $c_\alpha = -dV_\alpha/dt$, the constraint of the velocity of the center of masses of the entire system can be combined with other constraints.

[1] D. Frenkel and B. Smit, *Understanding Molecular Simulation From Algorithms to Applications*, 2nd ed. (Academic Press, San Diego, CA, 2002).

[2] D. C. Rapaport, *The Art of Molecular Dynamics Simulation*, 2nd ed. (Cambridge University Press, Cambridge, UK, 2004).

[3] K. Binder and D. W. Heermann, *Monte Carlo Simulation in Statistical Physics*, 5th ed. (Springer-Verlag, Berlin, 2010).

[4] S. Nosé, Mol. Phys. **52**, 255 (1984).

[5] W. G. Hoover, Phys. Rev. A **31**, 1695 (1985).

[6] G. Bussi, D. Donadio, and M. Parrinello, J. Chem. Phys. **126**, 014101 (2007).

[7] H. C. Andersen, J. Chem. Phys. **72**, 2384 (1980).

[8] G. J. Martyna, D. J. Tobias, and M. L. Klein, J. Chem. Phys. **101**, 4177 (1994).

[9] M. Parrinello and A. Rahman, J. Appl. Phys. **52**, 7182 (1981).

[10] D. J. Evans and G. Morriss, *Statistical Mechanics of Nonequilibrium Liquids*, 2nd ed. (Cambridge University Press, Cambridge, UK, 2008).

[11] B. D. Todd and P. J. Davis, *Nonequilibrium Molecular Dynamics* (Cambridge University Press, Cambridge, UK, 2017).

[12] M. S. Green, J. Chem. Phys. **22**, 398 (1954).

[13] R. Kubo, J. Phys. Soc. Jpn. **12**, 570 (1957).

[14] W. T. Ashurst and W. G. Hoover, Phys. Rev. A **11**, 658 (1975).

[15] A. W. Lees and S. F. Edwards, J. Phys. C: Solid State Phys. **5**, 1921 (1972).

[16] W. G. Hoover, D. J. Evans, R. B. Hickman, A. J. C. Ladd, W. T. Ashurst, and B. Moran, Phys. Rev. A **22**, 1690 (1980).

[17] D. J. Evans and G. P. Morriss, Phys. Rev. A **30**, 1528 (1984).

[18] E. M. Gosling, I. R. McDonald, and K. Singer, Mol. Phys. **26**, 1475 (1973).

[19] H. Bao, J. Chen, X. Gu, and B. Cao, ES Energy Environ. **1**, 16 (2018).

[20] A. Tenenbaum, G. Ciccotti, and R. Gallico, Phys. Rev. A **25**, 2778 (1982).

[21] P. K. Schelling, S. R. Phillpot, and P. Keblinski, J. Appl. Phys. **95**, 6082 (2004).

[22] J. Hickman and Y. Mishin, Phys. Rev. Mater. **4**, 033405 (2020).

[23] K. Tanaka, S. Ogata, R. Kobayashi, T. Tamura, and T. Kouno, Int. J. Heat Mass Transf. **89**, 714 (2015).

[24] T. Ikeshoji and B. Hafskjold, Mol. Phys. **81**, 251 (1994).

[25] D. J. Evans, Phys. Lett. A **91**, 457 (1982).

[26] M. J. Gillan and M. Dixon, J. Phys. C: Solid State Phys. **16**, 869 (1982).

[27] C. F. Gauss, J. Renie Angew. Math. **4**, 232 (1829).

[28] D. J. Evans, W. G. Hoover, B. H. Failor, B. Moran, and A. J. C. Ladd, Phys. Rev. A **28**, 1016 (1983).

[29] D. J. Evans and G. P. Morriss, Chem. Phys. **77**, 63 (1983).

[30] D. Brown and J. H. R. Clarke, Phys. Rev. A **34**, 2093 (1986).

[31] D. J. Evans, E. G. D. Cohen, and G. P. Morriss, Phys. Rev. Lett. **71**, 2401 (1993).

[32] H. A. Posch and W. G. Hoover, Phys. Rev. A **38**, 473 (1988).

[33] T. M. Galea and P. Attard, Phys. Rev. E **66**, 041207 (2002).

[34] E. R. Smith, D. M. Heyes, D. Dini, and T. A. Zaki, J. Chem. Phys. **142**, 074110 (2015).

[35] E. R. Smith, D. M. Heyes, D. Dini, and T. A. Zaki, Phys. Rev. E **85**, 056705 (2012).

[36] J. D. Weeks, D. Chandler, and H. C. Andersen, J. Chem. Phys. **54**, 5237 (1971).

[37] D. T. Lee and B. J. Schachter, Int. J. Comput. Inf. Sci. **9**, 219 (1980).

[38] A. F. Bower, *Applied Mechanics of Solids* (CRC Press, Boca Raton, FL, 2010).

[39] R. Penrose, Math. Proc. Cambridge Philos. Soc. **51**, 406 (1955).

[40] R. E. Rudd and J. Q. Broughton, Phys. Rev. B **58**, R5893 (1998).

[41] R. Kobayashi, T. Nakamura, and S. Ogata, Mater. Trans. **49**, 2541 (2008).

[42] M. R. Parsa, C. Kim, and A. J. Wagner, Phys. Rev. E **104**, 015304 (2021).

[43] O. G. Jepps, G. Ayton, and D. J. Evans, Phys. Rev. E **62**, 4757 (2000).

[44] A. Baranyai, Phys. Rev. E **62**, 5989 (2000).

[45] P. K. Patra and R. C. Batra, Phys. Rev. E **95**, 013302 (2017).

[46] W. C. Swope, H. C. Andersen, P. H. Berens, and K. R. Wilson, J. Chem. Phys. **76**, 637 (1982).

[47] R. Edberg, D. J. Evans, and G. P. Morris, J. Chem. Phys. **84**, 6933 (1986).

[48] A. Baranyai and D. J. Evans, Mol. Phys. **70**, 53 (1990).

[49] D. J. Braun and M. Goldfarb, Comput. Methods Appl. Mech. Eng. **198**, 3151 (2009).

[50] S. S. Khali, D. Chakraborty, and D. Chaudhuri, Soft Matter **17**, 3473 (2021).

[51] Y. Ishii, K. Sato, M. Salanne, P. A. Madden, and N. Ohtori, J. Chem. Phys. **140**, 114502 (2014).